Engineering Atomic Arrangement of Bimetallic Catalysts for Electrochemical CO₂ reduction

Linfeng Xie^a, Jiashun Liang^a, Cameron Priest^{b,c} Tanyuan Wang^a,

Dong Ding^{c,*}, Gang Wu,^{b,*} Qing Li^{a,*}

^aState Key Laboratory of Material Processing and Die & Mould Technology, School of Materials Science and Engineering, Huazhong University of Science and Technology, Wuhan 430074, China. ^bDepartment of Chemical and Biological Engineering, University at Buffalo, The State University of New York, Buffalo, NY 14260, United States

^cIdaho National Laboratory, Idaho Falls, ID 83415, United States

*Corresponding authors: dong.ding@inl.gov (D. Ding); gangwu@buffalo.edu (G. Wu); ging-li@hust.edu.cn (Q. Li)

Abstract: Electrochemical CO₂ reduction reaction (CO₂RR) to highly-valued chemicals is a sustainable solution to address environmental issues caused by excessive CO₂ emissions. Generally, the CO₂RR is challenging to achieve high efficiency and selectivity simultaneously due to multi-proton/electron transfer processes and complex reaction intermediates. Among studied formulations, bimetallic catalysts have attracted significant attention with promising activity, selectivity, and stability. Engineering the atomic arrangement of bimetallic nanocatalysts is a promising strategy for rationally designing structures (intermetallic, core/shell, and phase-separated structures) to improve catalytic performance. This review summarizes the recent

advances, challenges, and opportunities in developing bimetallic catalysts for the CO₂RR. In particular, we firstly introduce the possible reaction pathways on bimetallic catalysts concerning the geometric and electronic properties of intermetallic, core/shell, and phase-separated structures at the atomic level. Then, we critically examine recent advances in crystalline structure engineering for bimetallic catalysts, aiming to establish the correlations between structures and catalytic properties. Finally, we provide a perspective on future research directions, emphasizing current challenges and opportunities.

1.Introduction

Carbon dioxide (CO₂) is a greenhouse gas. Its increasing concentration in the atmosphere is the leading cause of global warming, responsible for destructive environmental consequences such as more frequent extreme weather events and sea-level rise.^{1,2} The accelerated consumption of fossil fuels has led to excessive emission of CO₂, with global CO₂ emissions from the burning of fossil fuels reaching 36.8 billion tons at the end of 2019.³ Also, in the early 1800s the atmospheric CO₂ concentration was ca. 270 ppm (parts per million), but has reached 407.8 ppm in 2018.⁴ Taking into account that the safety limit of CO₂ concentration in the atmosphere is estimated at 350 ppm, reducing the atmospheric CO₂ content is imperative.⁵⁻⁷ In recent years, to reduce the content of CO₂ in the atmosphere and convert it into value-added chemicals, various strategies such as thermochemical, electrochemical, and photochemical reductions have been extensively studied.⁸⁻¹² In particular, during the electrochemical CO₂ reduction reaction (CO₂RR), the change of

electrode potential could directly affect the adsorption of ions and the solvent's orientation at the electrode/solution interface, thereby regulating adsorption behaviors of reactants/intermediates and reducing the activation energy required for the CO₂RR.¹³ Furthermore, utilizing high efficient catalysts and optimal electrode potential can control the adsorption/desorption and electron transfer steps, allowing for tailoring reaction pathways and product selectivity.

CO₂ is a linear molecule with two equivalent C=O bonds (bond length = 1.12 Å).⁷ Since C=O has a high bond energy of 750 kJ mol⁻¹, breaking C=O bonds needs to overcome a substantial energy barrier and requires impractically high overpotentials.^{7,14}Additionally electrochemical CO₂ reduction involves multiple reaction intermediates and complicated proton-coupled electron transfer steps, leading to a broad product distribution including C₁ (e.g., CO,¹⁵ HCOOH,¹⁶ CH₄,¹⁷ CH₃OH, and HCHO), C₂ (e.g., C₂H₂, C₂H₆, C₂H₅OH, and CH₃COOH^{18, 19}), C₃ (e.g., C₃H₇OH²⁰), C₄ (e.g., C₄H₁₀²¹ and C₄H₈²¹), and C₅ (e.g., C₅H₁₂²¹) products. To this end, efficient electrocatalysts are the key to lower the reaction barrier and improve catalytic activity and selectivity.²²⁻²⁸

Among studied catalyst formulations,²⁹⁻³² numerous metallic catalysts for CO₂RR have been explored, which can be divided into the following three types according to their main products: CO (on Ag, Au, Zn, etc.),^{33, 34} formate (on Bi, Sn, Hg, In, etc.),³⁵⁻³⁷ and hydrocarbons (on Cu).^{18, 38} In principle, the catalysts' electronic and geometric structures could determine the adsorption energy of reaction intermediates, which can significantly affect the reaction pathway and the resulting products of the CO₂RR. For example, the p-electron distribution dominant metals such as Bi, In, Sn, Pb, and their oxides lead to strong adsorption of CO₂ and prevents its further

reduction, resulting in the preferrable generation of HCOOH.^{35, 39, 40} Au and Ag can selectively produce CO due to their weak adsorption towards the *CO intermediate.³⁴ Cu can produce hydrocarbons due to its moderate binding energies with *CO that makes subsequent hydrogenation and C-C coupling possible. 18 However, the efficiency and selectivity of most monometallic catalysts for the CO₂RR are unsatisfactory.^{39, 41, 42} Therefore, extensive studies on bimetallic alloy catalysts with disorderly solid solution structures were explored for the CO₂RR.^{33, 43} To further improve catalytic performance, engineering the atomic arrangement of bimetallic alloy nanocatalysts for rationally designing are promising strategies concerning three major categories: (1) intermetallic ordered structure, (2) core/shell structure, and (3) phase-separated structure. Intermetallic ordered structures are generally more thermodynamically stable than their disordered counterparts and could provide a unique electronic structure and well-defined coordination environment, thereby enhancing catalytic activity and stability. 44-48 The core/shell structure is another kind of atomic configuration to regulate catalytic properties via surface strains caused by the lattice mismatch between core and shell. 13 The induced surface strain can effectively modulate electronic structures of shell components and enhance the catalytic activity. In phase-separated structures, the two phases are separated by distinct grain boundaries. The phase boundary may be distorted or defective due to the lattice mismatch of the two phases. There may be a synergistic effect between the two phases at the interface, which could offer specific adsorption sites for CO₂/intermediates and improve the electrocatalytic efficiency.

This review elaborates on the principles and applications of improving CO₂RR performance

via atomic arrangement engineering of bimetallic electrocatalysts. Firstly, the possible reaction pathways of the CO₂RR on bimetallic catalysts are introduced concerning three atomic arrangement engineering strategies (intermetallic, core/shell, and phase-separated structures). Secondly, recent advances in enhancing CO₂RR activity and selectivity are critically examined, focusing on bimetallic catalysts' engineering atomic arrangements. Finally, current challenges, perspectives, and opportunities in developing bimetallic catalysts for the CO₂RR are outlined.

2. Mechanism and atomic arrangement engineering

2.1 Mechanism of the electrochemical reduction of CO₂

The product selectivity of the CO₂RR depends not only on the type of catalyst and its surface electronic/geometric configurations but also directly related to the electrodes' potential. At room temperature and a pH of 7, the primary reactions of the CO₂RR and their corresponding redox potentials are shown in Table 1. Various C₁-C₃ products can be obtained through 2, 4, 6, 8, 12, and 18 electron transfer pathways.

Table 1. Typical CO₂RR pathways to produce various products and their corresponding redox potentials.

Reaction	Potential	
$CO_2 + H_2O + 2e^- \rightarrow CO + 2OH^-$	-0.52 V vs. SHE	
$CO_2 + H_2O + 2e^- \rightarrow HCOO^- + OH^-$	-0.43 V vs. SHE	
$CO_2 + 3H_2O + 4e^- \rightarrow HCHO + 4OH^-$	-0.51 V vs. SHE	
$CO_2 + 5H_2O + 6e^- \rightarrow CH_3OH + 6OH^-$	-0.38 V vs. SHE	
$CO_2 + 6H_2O + 8e^- \rightarrow CH_4 + 8OH^-$	-0.24 V vs. SHE	
$2CO_2 + 8H_2O + 12e^- \rightarrow C_2H_4 + 12OH^-$	-0.34 V vs. SHE	
$2CO_2 + 9H_2O + 12e^- \rightarrow C_2H_5OH + 12OH^-$	-0.33 V vs. SHE	
$3\text{CO}_2 + 13\text{H}_2\text{O} + 18\text{e}^- \rightarrow \text{C}_3\text{H}_7\text{OH} + 18\text{OH}^-$	-0.32 V vs. SHE	

Generally, the CO₂RR involves three primary elemental steps. The first is the CO₂ adsorption on active sites with optimal strength. Then CO₂ is activated along with electron/proton transfers to form various intermediates and products. Next, desirable product desorption occurs to recover active sites for a new cycle.²⁹ Fig. 1(a-c) summarizes the reaction mechanisms of CO₂ reduction at different catalyst surfaces. Pb, Tl, Sn, Hg, In, Cd, and Bi can catalyze CO₂ to form formic acid.⁴⁹⁻⁵² The adsorbed CO₂ obtains one electron. It interacts with *H (on Pb, Bi)⁵³ or *OH (on Sn, In)⁵⁴ to generate adsorbed bicarbonate species further reduced to either *OCHO or *COOH.³⁹ Then it gets another electron and desorbs from the catalyst surface to form HCOOH or HCOO⁻(Fig. 1a).⁵⁵⁻⁵⁷

CO can be obtained by using Au, Ag, Zn, Pd, and Ga as catalysts.^{33, 34, 58-61} CO₂ molecules are adsorbed at the surface of the catalyst and form C terminal intermediates. Reduction of CO₂ to CO proceeds through a *COOH intermediate.⁶² The formation of this intermediate can occur in one of the following ways: (i) one-step proton-coupled electron transfer (PCET), or (ii) a single electron transfer to form *COO-, and further protonation to obtain *COOH.⁶³ Then *COOH is

hydrogenated and then dehydrated to form *CO and H_2O , which desorbs from the catalyst surface to form the gas-phase CO (Fig. 1b).^{41,57}

Cu used to be the only catalyst that can generate hydrocarbons due to its moderate adsorption of *CO intermediates. *43,64-67* The *CO intermediate obtains one electron and interacts with *H (on Cu) to generate the *COH intermediate or *CO, followed by direct dimerization to form *OCCO. The *COH intermediate and *CO intermediate are coupled through C-C to form *COCOH, which is then hydrogenated and dehydrated before desorbing from the catalyst surface to form C₂H₄. Alternatively, a *COH intermediate can also form C₂H₄ by direct hydrogenation and then dimerization. The *OCCO intermediate obtains electrons and interacts with *H to form C₂H₅OH or dehydrates to form C₂H₄. C₂H₆ can be generated by *COH intermediate dimerization after complete hydrogenation or C₂H₄ hydrogenation (Fig. 1c). *43, 68-71* According to the above possile mechanisms of the CO₂RR, the electronic/geometric structures of catalysts are the key to determining the adsorption behaviors of CO₂ and intermediates, which can be regulated through atomic arrangement engineering.

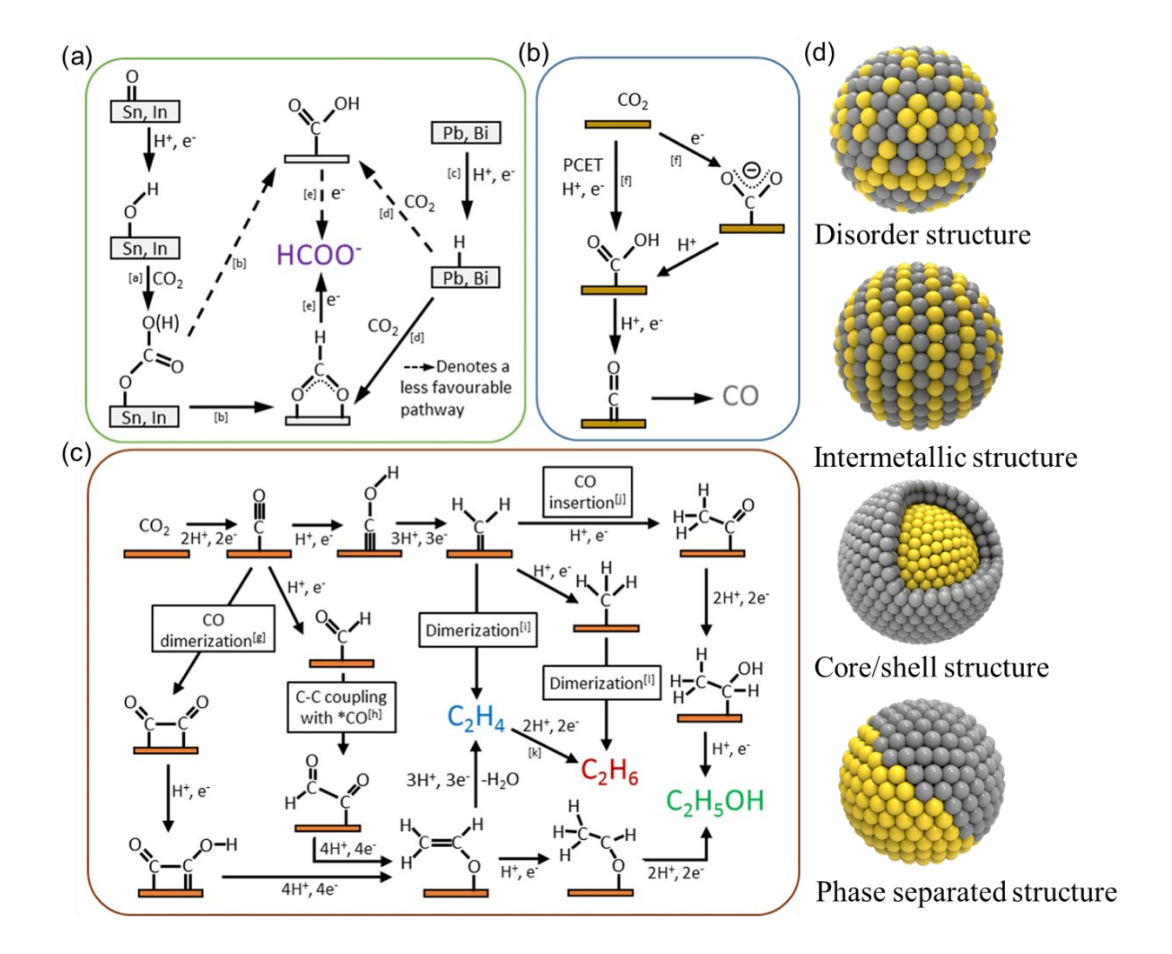


Fig. 1. The reaction mechanisms of the CO₂RR on different catalysts to produce (a) formate, (b) CO, and (c) hydrocarbons. Reproduced with permission.⁷² Copyright 2018, Elsevier. (d) Schematic illustration of four kinds of atomic engineering arrangements for the CO₂RR.

2.2 Tuning adsorption and electronic effects through atomic arrangement

The adsorption strength of molecules at the surface of metal catalysts is usually expressed by adsorption energy (AE) or binding energy (BE) as follows:⁷³

$$AE = E_{M-A} - E_M - E_A$$

Among them, E_{M-A} is the energy of the system after bonding the adsorbate with the metal surface,

while E_M and E_A are the energy of the metal surface and the adsorbate, respectively. Hammer and Norskov^{74, 75} proposed the *d*-band center theory that the catalyst's catalytic activity is determined by the binding energy of the surface and the reaction intermediate, which is closely related to the *d*-band center of the catalyst. According to this principle, a secondary metal is usually introduced into the pristine one to adjust the *d*-band center of the binary alloy and modify intermediates' binding energies, which can optimize catalytic activity and selectivity.

Engineering the atomic arrangement of general binary alloys through forming disordered solid solution structures could fine-tune the local electronic and geometric structures of active sites towards catalytic performance enhancement. The schematic illustration of four types of atomic engineering arrangements is shown in Fig. 1d. For instance, as a long-term ordered structure, intermetallic compounds show different physical and chemical properties from the disordered ones. The following formula can explain the Gibbs free energy change of disorder-order transformation

$$\Delta G_{d \to o} = \Delta H_{d \to o} - T \Delta S_{d \to o}$$

Where d and o represent disordered and ordered phases, respectively. Disordered alloys have a negative value of $T\Delta S_{d\to o}$ due to the higher entropies than ordered ones. ⁷⁶ As a result, at high temperatures $T\Delta S_{d\to o}$ dominates and is not favorable for the disorder-order transition. At relatively low temperatures, $\Delta G_{d\to o}$ is determined by $\Delta H_{d\to o}$, related to composition and bond energy as given below:⁷³

$$\Delta H_{d\to o} = X_A X_B \varepsilon$$

$$\varepsilon = \varepsilon_{AB} - \frac{1}{2}(\varepsilon_{AA} + \varepsilon_{BB})$$

where X_A and X_B are molar fractions of A and B in the A-B alloy, respectively; ε represents the bond energy difference between the average energies of A-A (ε_{AA}) and B-B (ε_{BB}) bonds and A-B bond (ε_{AB}). In ordered structures, the strong d orbital interaction and A-B bonds lead to negative values of ε and thus $\Delta H_{d\to o}$. The above two equations indicate that $\Delta H_{d\to o}$ and the corresponding $\Delta G_{d\to o}$ will be determined by the type and composition of A-B alloy.

Due to their definite composition and structure, intermetallic structures could provide predictable control over local coordination environments (e.g., bond length) and electronic structures of bimetallic catalysts. In our study, the intermetallic structure, as a thermodynamically stable structure⁷⁷, may not only render strain effects during the disorder-order transition, but also tune the bond length in such a way to optimize the catalytical activity. ⁷⁸ For example, in L1₀-PtZn intermetallic catalysts, biaxial strains including a compression along <011> and <101> directions and a tension along <110> direction are induced after fcc-L1₀ phase transformation, thereby promoting their oxygen reduction reaction (ORR) activity. ⁷⁹ Besides, the Pt-Pt bond length in L1₀-PtCoW (2.707 Å) is shorter than that of Pt foil (2.765 Å). The shortened Pt-Pt bond and the resultant compressive strain on the surface could weaken the Pt-O bonding and enhance the ORR activity.80 The ordered Pt₃Co's unit cell comprises a periodic square array where eight Pt atoms surround each Co atom, which has a favorable d-band center and spin density distribution compared to the disordered ones, leading to enhanced activity for the ORR. 81, 82 Furthermore, since the order of intermetallic phase arises from the high mixing enthalpy, a higher chemical and structural stability can be expected than disordered alloys. 65, 78-80, 83-87

Constructing core/shell structures is another atomic arrangement engineering, which receives great attention. The strong ligand and strain effects between the core and shell provide an effective way to modulate the surface environment's electronic structure.⁸⁸ The lattice mismatch at the core/shell interface will produce a strain effect, bring compressive or tensile to the surface atoms.⁸⁹⁻⁹² Surface ligand effect is a short-range effect, mainly existing in the two or three atomic layers on the surface. In addition to the above two effects, there are also geometric effects that can regulate the surface reactivity, such as vacancies and defects.^{59,93} Through surface engineering, shell layers with abundant vacancies or specific metal dopants can be accurately constructed, improving CO₂RR activity and selectivity.⁹⁴

Phase separated structure is the creation of two distinct phases from a single homogeneous mixture. Heterogeneous phases with different chemical properties could form a synergistic effect and reduce the electron migration distance at the phase interface, resulting in improved catalytic activity and product selectivity. Heterogeneous synergies can be expressed as follows:

$$M_a - A_{ad} + M_b - B_{ad} = M_a + M_b + A_{ad} - B_{ad}$$

Where A_{ad} , B_{ad} denote two different adsorption intermediates and M_a , M_b denotes two different metal adsorption sites. The prerequisite for completing this reaction is that the catalyst's surface requires multiple adsorption sites (or reaction sites) to participate in the reaction. The phase separation structure induces a heterogeneous synergistic effect at the two-phase interface to influence the catalytic performance. ^{17,95} For instance, in the Pd-Rh nanobox catalyst, the migration

of Pd between Rh columns in the shell creates a phase-separated and strained heterostructure, which lowers the d-band center, promotes the desorption of *O and *OH from the metal surface and thus enhances the activity. ⁹⁶

With the development of atomic arrangement engineering, the structure, size, composition, and morphology of the catalyst can now be designed to achieve high-efficiency catalysis. This review focuses on the recent three types of nanocatalysts with atomic arrangements engineering and highlights their morphological/structure-dependence on CO₂RR electrocatalysis.

3. Intermetallic bimetallic nanocatalysts for the CO₂RR

3.1 Au-based intermetallic nanocatalysts

Precious metal catalysts, such as Au and Ag, can reduce CO₂ to CO due to their weak adsorption capability to *CO intermediates. However, its high cost and negative onset potential still need to be resolved. Introducing non-noble metals can adjust the *d*-band center to tune metal and intermediates' binding and reduce catalyst cost. Ordered AuCu intermetallic nanoparticles (NPs) of 1:1 atomic ratio with 7 nm were synthesized by the reduction of Cu(CH₃COO)₂ on the preformed Au seeds.⁹⁷ The degree of ordering in Au/Cu NP structures is controlled by reaction temperature and duration (Fig. 2a). The superlattice peaks in the X-ray diffraction (XRD) pattern (Fig. 2b), which do not exist in the disordered AuCu alloy (d-AuCu), become more evident in the ordered NPs. High-angle annular dark field-scanning transmission electron microscopy (HAADF-STEM) images of ordered intermetallic AuCu (o-AuCu) sample clearly shows a periodic

oscillation of intensity due to the Z-contrast difference between Au (bright atom) and Cu (dark atom) in an ordered lattice (Fig. 2c). During the CO₂RR, o-AuCu has the highest Faradaic efficiency of CO (FE_{CO}) (75%) at -0.77 V vs. reversible hydrogen electrode (RHE) compared to other samples with less ordered structures (Fig. 2d). Moreover, the o-AuCu NP catalyst is more stable than d-AuCu NPs, with no apparent FE drop after a 12 h test. Comparing the thermodynamic limit potential (U_L) for CO₂ reduction and H₂ evolution of three model systems, U_L (CO₂) and (U_L(CO₂)-U_L(H₂)) of the o-AuCu NP is the most positive compared to Au and d-AuCu, which accounts for its highest CO₂ to CO conversion activity and selectivity.

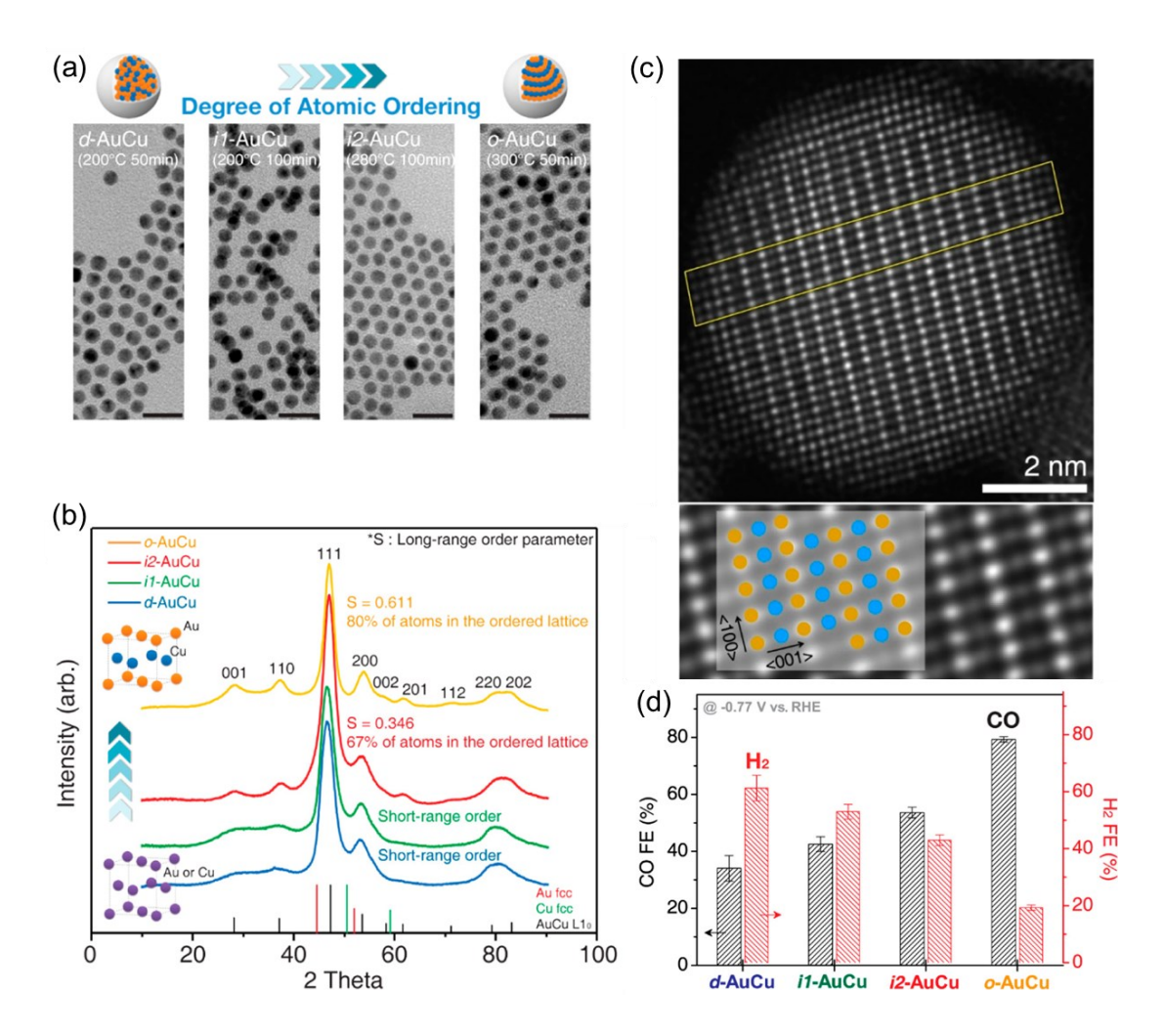


Fig. 2. (a) TEM images and (b) XRD patterns of AuCu NPs with different ordering degree. (c) HAADF-STEM image and magnified STEM image of o-AuCu. (d) FE_{CO} of AuCu NPs with different ordering degrees at -0.77 V vs. RHE. Reproduced with permission.⁹⁷ Copyright 2017, American Chemical Society.

An intermetallic Au₃Cu alloy nanocrystal (NC) catalyst was prepared and studied for the CO₂RR.⁹⁸ By controlling the amount of Au in the precursor, the prepared Au₃Cu alloy NC size can be adjusted in a range from 15 to 30 nm. The onset potential of Au₃Cu NCs (-0.9 V vs. Ag/AgCl)

was more favorable than those of the Au NPs (-1.15 V vs. Ag/AgCl), significantly enhancing the CO₂RR activity. At - 1.6 V, Au₃Cu NCs have a distinctive selectivity toward CH₄ with 40% higher FE than Au NPs. Besides, AuSn intermetallic NPs at the size of 23-33 nm were prepared by chemical reduction of Sn precursor in the presence of pre-made Au NPs. ⁹⁹ The onset potential of formate on the intermetallic AuSn was significantly shifted to a positive potential (-0.4 V vs. RHE), compared with that of Sn foil (-0.8 V vs. RHE). At -1.1 V vs. RHE, the total current density on the intermetallic AuSn reaches 12 mA cm⁻², which is twice and three times that of Au and Sn foils, respectively. Raman spectroelectrochemistry and isotopic labeling experiments prove that bicarbonate anions at the electrode surface are the primary CO and formate source. The improved catalytic performance on the intermetallic AuSn might be related to the changes of adsorption sites, surface energy, and orientation of adsorbates.

3.2 Cu-based intermetallic nanocatalysts

Currently, Cu is probably the only metal electrocatalyst to reduce CO₂ to hydrocarbons but typically has an undesirably wide range of product distribution. Norskov et al. ¹⁰⁰ predicted that the bimetallic Cu-based catalyst might break the scaling relationship and stabilize the reaction intermediate to reduce the overpotential and improve the selectivity. For example, alloying with a high oxygen affinity metal that geometrically interacts with the plane geometry of the *CHO site but not with the plane geometry of the linear *CO site could stabilize complex compounds. Therefore, such Cu alloys catalysts could reduce the energy of CHO* relative to CO* and

favorably improving the selectivity to C_1 or C_2 hydrocarbon products. This section summarizes the current research on binary Cu-base intermetallic compounds and highlights their merits in improving product selectivity and efficiency.

The effect of different CuPd structures on catalytic performance and product selectivity for the CO₂RR was recently explored.⁶⁵ CuPd NPs of 1:1 atomic ratio with disordered, ordered, and phase-separated structures were prepared through co-reduction of Pd(II) acetate and Cu(II) acetate by using NaBH4. High-resolution transmission electron microscope (HR-TEM) image and XRD (Fig. 3a-b) show that the intermetallic CuPd NP contains the ordered B2 structure,¹⁰¹ consisting of interconnected crystals with a particle size of ~50 nm. During the CO₂RR, the ordered CuPd catalyst shows the highest FE_{CO} of 80% at -0.53 V (vs. RHE), while the phase-separated CuPd mainly produced C₂H₄ with a FE of 50% at -0.74 V (Fig. 3c-d). Surface valence band photoemission spectra indicated that, besides the catalysts' d-band position, geometric/structural effects such as orientations of the intermediate on the Cu-Pd surface leads to different selectivities.

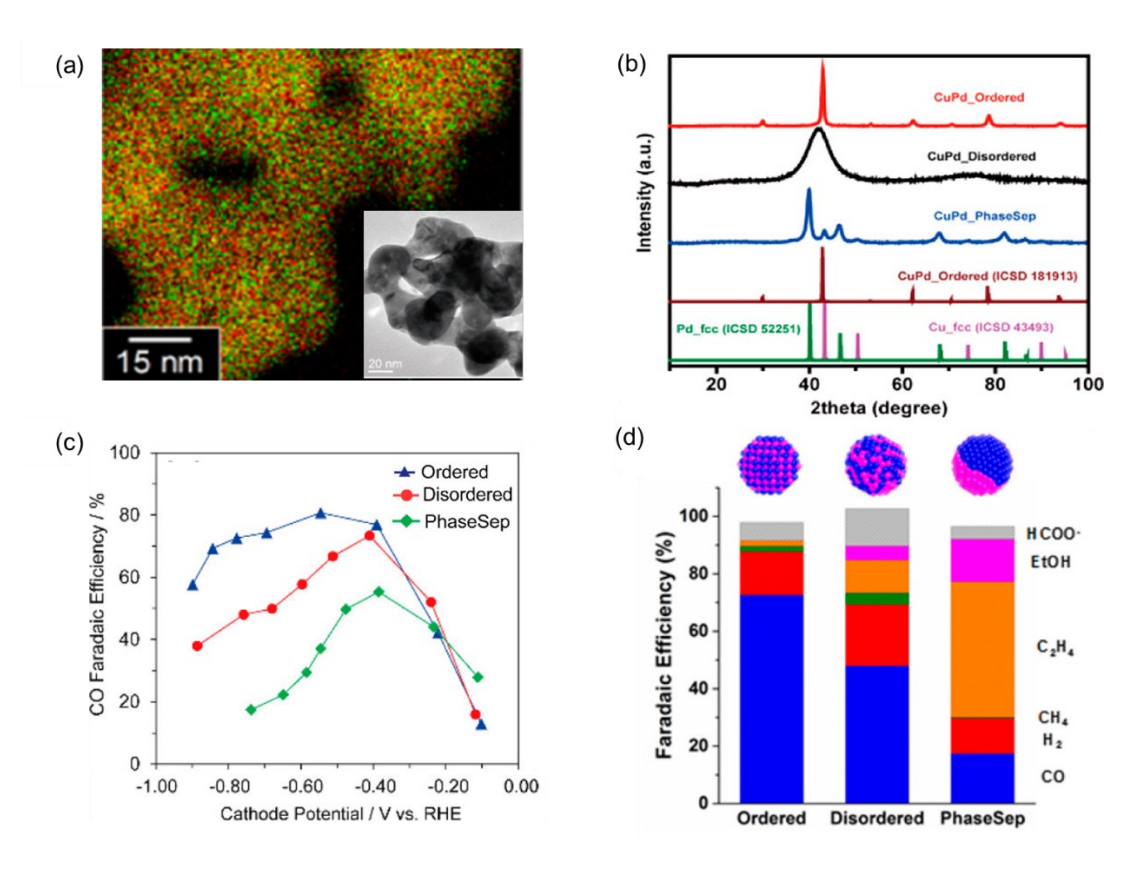


Fig. 3. (a) EDS elemental mapping of ordered CuPd NPs (Cu-red and Pd-green). Insets: TEM image of the corresponding area. (b) XRD patterns of different structured CuPd NPs. (c) The FEco and (d) total FEs of random alloy, ordered intermetallic and phase-separated CuPd NPs. Reproduced with permission. ⁶⁵, Copyright 2017, American Chemical Society.

3.3 Ni-based intermetallic nanocatalysts

Recently, certain intermetallics that do not contain Cu were identified for reducing CO₂ to multicarbon products. Studies on intermetallic Ni_xGa_y film demonstrated that the Ni-based ordered alloy could reduce CO₂ to C₂ products. Three different phases (e.g., NiGa, Ni₃Ga and Ni₅Ga₃) consisting of aggregated intermetallic particles in a size range of 1-5 µm were prepared by using the drop-casting method. The onset potential of Ni₅Ga₃ to reduce CO₂ to C₂ products (ethylene and ethane) is 250 mV positive than that of polycrystalline Cu and is approximately equal to that of single-crystalline Cu. Specifically, polycrystalline Cu produced only CO and HCOO⁻ in the range of -0.5 V to -0.85 V, while Ni_xGa_y intermetallic phases generated CH₄, C₂H₄, and C₂H₆ within an identical potential range. The introduction of Ga into the Ni films could weaken the Ni-CO interaction, mitigate surface poisoning, and improve the yield of highly reduced products.¹⁰³

Intermetallic Ni₃Al alloy thin films as CO₂RR catalysts were synthesized on glass carbon (GC) substrate by sing drop-casting and furnace reduction procedure method. ¹⁰⁴ Intermetallic Ni₃Al film could reduce CO₂ to hydrocarbon products, with 1.9 ± 0.3% of FE_{1-propanol} and 1.0 ± 0.2% of FE_{methanol} at -1.38 V vs. Ag/AgCl. Also, the Ni₃Al film can reduce CO₂ to CO with an FE of 33% at -1.38 V. When CO is fed as the reactant instead of CO₂, the production rate of methanol increases exponentially. However, the propanol's production rate is limited to the accumulation of three neighboring adsorbed *CO molecules at the catalyst surface. Thus, the rate still presents a linear trend. Exactly how to eliminate the rate-limiting step of conversion from CO₂ to CO is a key to improving the efficiency of the Ni₃Al catalyst.

The catalytic properties of recently reported bimetallic intermetallics for the CO₂RR are summarized in Table 2. In this section, we discuss three categories of intermetallic compounds as catalysts for CO₂RR. Among them, Au-Cu and Cu-Pd systems reveal excellent catalytic efficiency and product selectivity towards the CO. Although the Ni-based intermetallic catalysts could produce hydrocarbon products, efficiency and selectivity need to be further improved. Generally,

the progress of applying intermetallic catalysts for the CO₂RR is still in the early stage. The main reason for the low efficiency of hydrocarbon production on intermetallic catalysts may be the lack of accurate atomic structure controls. The bulk structure is converted into an ordered one, but surface layers are still partially disordered. The binding energy of the key reaction intermediate for generating hydrocarbons, such as *CO, may be not optimized yet, making the subsequent hydrogenation and/or C-C coupling difficult to proceed. In future research, the electronic and geometric structures of the intermetallics' catalyst surface should be fine-tuned, aiming to tailor the adsorption/desorption energy of key intermediates and the resulted reaction pathways. Surface segregation or defects should be explored to create new active sites. Bulk intermetallic structures can affect the surface catalytic properties by ligand and/or strain effects. Importantly, theoretical predictions are critical for rational catalyst design and synthesis with improved catalytic activity and selectivity for the CO₂RR.

Table 2. Summary of representative intermetallic catalysts for CO₂RR.

Intermetallics	Main products	Efficiency	Potential	Refs.
AuCu	СО	75%	-0.77 V vs RHE	89
Au ₃ Cu	CH ₄	40%	-1.6 V vs Ag/AgCl	90
AuSn	НСООН	42%	-1.1 V vs RHE	91
CuPd	CO	80%	-0.53 V vs RHE	58
Ni ₅ Ga ₃	CH ₄	2%	-0.88 V vs. RHE	94
	C_2H_6	1.75%	-0.88 V vs. RHE	

Ni ₃ Al	C_3H_7OH	$1.9 \pm 0.3\%$	-1.38 V vs	96
			Ag/AgCl	
	CO	33%	-1.38 V vs	
			Ag/AgCl	

4. Core/shell structured bimetallic nanocatalysts for CO2RR

4.1 Metal/metal core/shell structures

Core/shell structures with different metal cores and shells are a common catalyst configuration. For instance, Au and Pd can both reduce CO₂ to CO individually. At the Au surface, the activation of CO₂ to *COOH has a large energy barrier, but the desorption of *CO is easier. In contrast, at the Pd surface, the trend is reverse. 105 Aiming to improve the activity and selectivity for the CO formation by using both metals in a single catalyst, 7.5 nm Au/Pd core/shell NPs with 2-3 atomic layered Pd shells were synthesized by using a one-pot method (Fig. 4a-b). 106 As for the CO₂RR (Fig. 4c), the FE_{CO} of Au/Pd NPs with different Au/Pd compositions were all greater than 90% in a wide potential range, of which the FE_{CO} of Au₆₀Pd₄₀ NPs reaches a maximum of 96.1% at -0.7 V vs. RHE, significantly better than individual Au or pure Pd metal catalysts. DFT calculations (Fig. 4d) predicted that, compared to pure Pd (0.18 eV) and Au (0.98 eV), the associated free energy change of CO₂ to *COOH in AuPd NPs (0.08 eV) is significantly reduced. Additionally, the adsorption energy of hydrogen deviated more negatively by 0.06 eV in AuPd NPs than on Pd, which could suppress the HER.

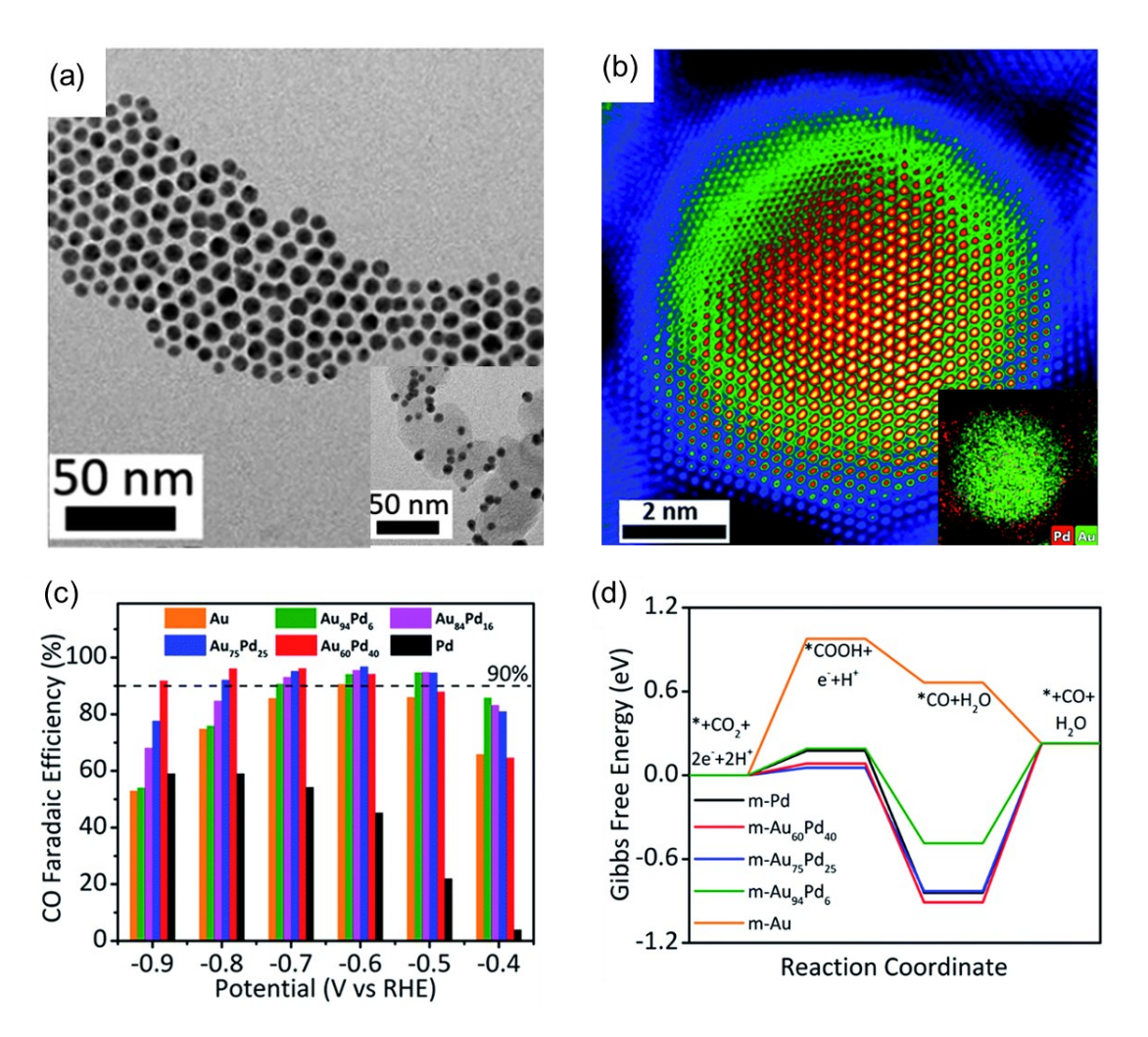


Fig. 4. (a) TEM images of synthesized Au₆₀Pd₄₀ NPs and corresponding NPs loaded on carbon black (insets). (b) Colored HAADF image and XEDS element mapping (insets) of Au₆₀Pd₄₀ NPs. (c) The FE_{CO} of all synthesized Au-Pd core/shell NPs. (d) DFT calculations, free energy diagrams for CO₂RR. Reproduced with permission. ¹⁰⁶ Copyright 2019, American Chemical Society.

 180 ± 20 nm Ag/Cu core/shell NPs were prepared by reducing mixtures of AgNO₃ and Cu(OAc)₂·H₂O in ethylene glycol in the presence of PVP at 180 °C. 107 Cu shells with a thickness

of 15 ± 3 nm were partially overgrown on the Ag core for Ag/Cu-20 (20 min of heating time). In electrochemical performance tests, the Ag/Cu yielded the highest FE_{CO} of 82% at -1.06 V vs. RHE, better than Ag NPs with 78% of FEco. Under the same potential, Ag/Cu has 28.6% ethylene generation, showing higher selectivity than Ag. When the Cu content is low, the stability of *COOH can be enhanced with Cu content, which manifests itself in the improvement of CO efficiency. Due to the formation of a certain thickness of Cu shells, the lattice mismatch between Ag and Cu atoms generates tensile stress at the surface, resulting in an enhancement of *CO adsorption and the subsequent hydrocarbon formation. This similar phenomenon can also be observed in the Au/Cu core/shell NPs. 108 It has the highest ethylene selectivity with 7-8 layers of Cu and the highest methane selectivity at 15 layers of Cu. When the number of Cu layers is smaller, the tensile strain will increase *CO and the subsequent C₂H₄ formation. With an increase in the number of Cu layers, tensile strain is weakened, and methane would be obtained as the dominant product.

4.2 Metal/metal compound core/shell structures

Apart from the metal shell, metal compounds can also have synergistic effects with the metal core to affect the performance of the CO₂RR. Compared to the metal/metal core/shell structure, the metal/metal compound core/shell structures may create new active sites due to the electrochemical reduction of the metal compound shells during the CO₂RR.

Cu-SnO₂ could be reprocessed to form different structures to study their structure-dependent

CO₂RR performance. The prepared Cu-SnO₂ core/shell NPs were annealed at 250 °C for 1 h with three strategies: (1) in air, (2) in H₂/N₂, and (3) firstly in air then in H₂/N₂ to obtain hollow heterostructure, core/shell structure, and hollow Janus structure, respectively (Fig. 5a). 109 As shown in Fig. 5b-c, the Cu-SnO₂ catalyst with hollow heterostructure had the best product selectivity and efficiency, reaching a 70% FEco and 71.5% FE_{HCOOH} at -0.7 and -1.0 V vs. RHE, respectively. During the CO₂RR, the reaction free energy of COOH* species was decreased at a large number of Cu/SnO₂ interfaces, thus improving the selectivity of HCOOH. DFT calculations (Fig. 5d) predicted that the interfaces of Cu/SnO₂ can reduce the free energy of *COOH species formation to 0.52 eV, lower than those of the Cu (111) surface (0.71 eV) and SnO₂ (110) surface (2.32 eV). Therefore, it can quickly transform *COOH to *CO and then desorb to form CO at a lower free energy of -0.13 eV. Also, the core/shell Cu/SnO₂ nanowire structures were prepared by annealing it in air, H₂ /N₂, and N₂ (Fig. 5e). 94 Cu/SnO₂ core/shell NWs after annealing in air achieved the best HCOOH selectivity than the samples annealed in H_2/N_2 and N_2 at -1.0 V vs. RHE, with the maximum FE_{HCOOH} reaching 90.2%.

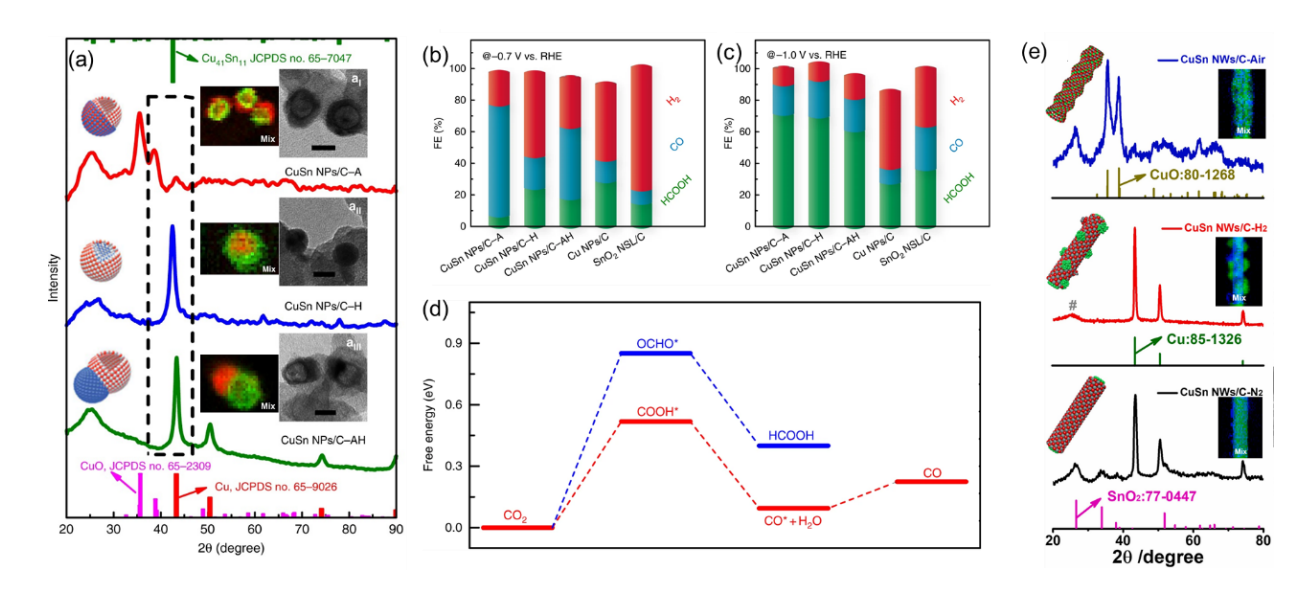


Fig. 5. (a) XRD patterns, TEM images, and elemental mappings of Cu/SnO₂ NPs after different annealing treatments. (b-c) FEs for CO, H₂ and HCOOH at (b) -0.7 V vs. RHE and (c) -1.0 V vs. RHE for different catalysts. (d) Free energy profiles of two pathways for CO₂ electroreduction on Cu/SnO₂ interfaces. (a-d) Reproduced with permission. Copyright 2018, Nature Publishing Group. (e) XRD patterns and elemental mappings of Cu/SnO₂ nanowires after different annealing treatments. Reproduced with permission. Copyright 2019, Elsevier.

We designed Cu/SnO₂ core/shell structured catalysts and studied their SnO₂ thickness-dependence on CO₂RR activity.¹³ Monodisperse core/shell Cu/SnO₂ NPs were prepared by using a seed-mediated method via a reduction of Sn(acac)₂ in the presence of 7 nm Cu NP seeds at 250°C for 1 h (Fig. 6a). The CO₂RR activity and selectivity of the Cu/SnO₂ NPs are closely related to the thickness of the SnO₂ shell (Fig. 6b-c). The thinner SnO₂ (0.8nm) layer is selectively active for the formation of CO₂ and its FE reaches 93% at -0.7 V vs. RHE. In contrast, Cu/SnO₂ NPs with thicker

SnO₂ (1.8 nm) shells tend to predominantly form HCOOH like SnO₂ (FE of 85% at -0.9 V vs. RHE). DFT calculations (Fig. 6d) elucidated that the excellent CO selectivity on the 0.8 nm SnO₂ shell is due to the synergistic effects between 10% uniaxial lattice compression and Cu atom doping lowers the energy barrier for CO formation. Such a synergistic effect was also observed on 7 nm core/shell Cu/In₂O₃ NPs for tunable syngas formation from the CO₂RR.¹¹¹ By controlling the thickness of the shell layer and the applied potential (-0.4 to -0.9 V vs. RHE), a wide H₂/CO ratio (4/1 to 0.4/1) can be obtained with a FE of the syngas greater than 90%.

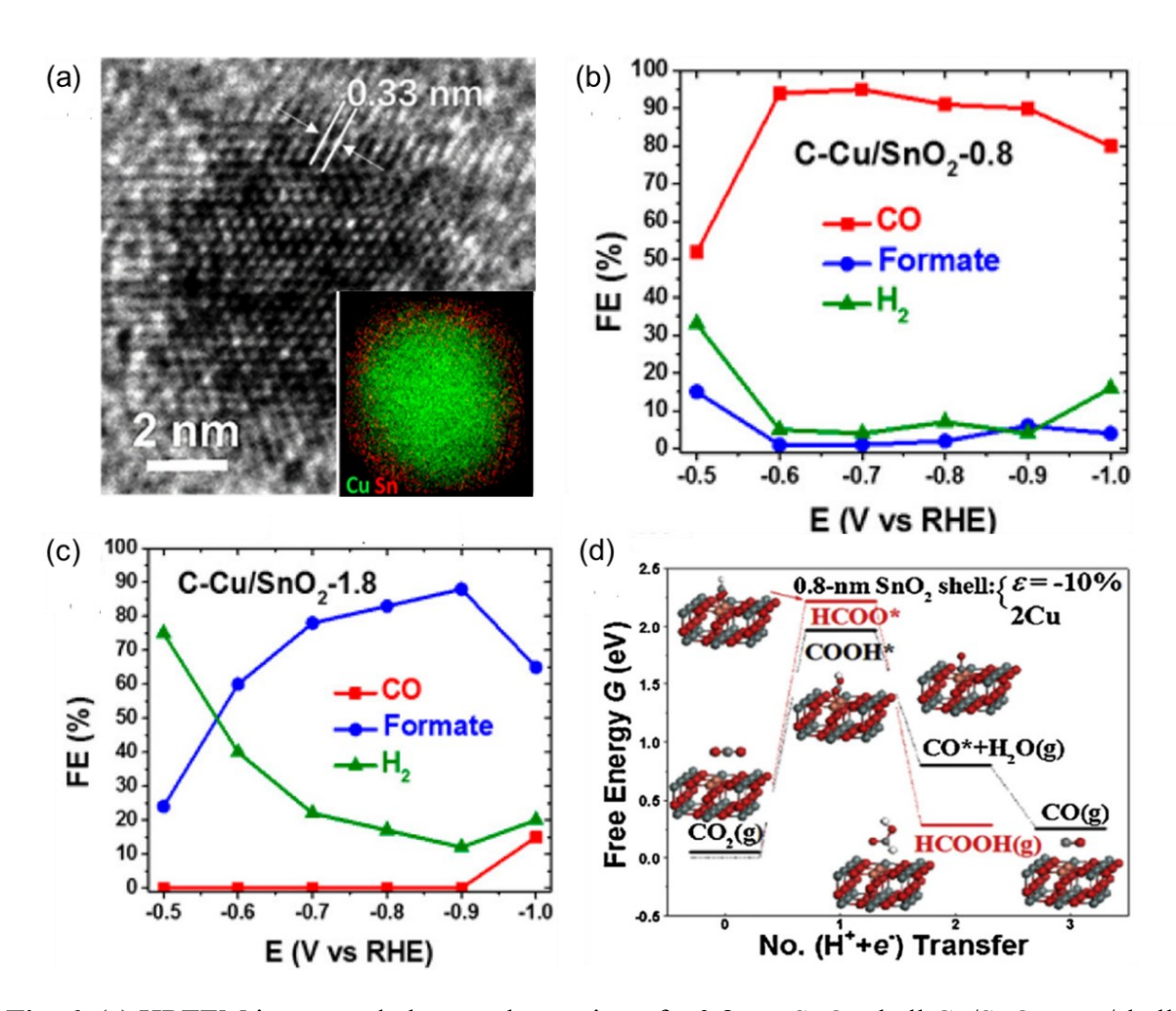


Fig. 6. (a) HRTEM image and elemental mapping of a 0.8 nm SnO₂ shell Cu/SnO₂ core/shell NP.

(b-c) FEs for CO, H₂ and HCOOH on (b) C-Cu/SnO₂-0.8 nm and (c) C-Cu/SnO₂-1.8 nm catalysts.

(d) Calculated free energies of two reaction paths on a 0.8 nm-SnO₂ shell with 2 Cu atoms on the surface and 10% uniaxial compression. Reproduced with permission. Copyright 2017, American Chemical Society.

Designing core/shell structured catalyst with Cu compound in the shell has been studied for the CO₂RR due to the high selectivity towards C₂ products in valence Cu surface. A core/shell Cu/Cu₂O nanorod catalyst with Cu/Cu⁺ interface was prepared by exposing Cu to air at ambient conditions for three weeks. 112 The Cu/Cu₂O core/shell nanorod has a coral-like microstructure with a diameter of 100 nm. Previous research suggests that the C atom of the intermediate *CO at the Cu⁺ surface is positively charged, while the C atom on the Cu⁰ surface is negatively charged. 113 Thus, in the core/shell Cu/Cu₂O catalyst, the two kinds of C atoms may exhibit electrostatic adsorption to form a dimer (Fig. 7a). The Cu/Cu₂O catalyst shows that the total FE of C₂ products can reach 50% under -1.0 V vs. RHE and the maximum yield of ethylene can reach 45% (Fig. 7b). A possible issue is that the surface Cu⁺ can be easily reduced to Cu⁰ during the CO₂RR. The introduction of heteroatoms could stabilize surface Cu⁺. Sargent's team prepared Cu/CuB core/shell nanostructures by wet-chemical methods and reported the effects of different Cu oxidation states on hydrocarbon production.⁸⁵ With the change of B's doping concentration, the average oxidation state of Cu can be adjusted in the range from 0 to +1 due to the electron transfer from Cu to B in CuB. The electrochemical test shows that Cu with an average valence state of +0.35 has the best performance, and the FE of C_2 products reached 79%. In the 40h electrochemical test, the ethylene FE remains stable (keeping above 45%) (Fig. 7c). DFT calculations suggest B's doping can inhibit the reaction path to C_1 products and increase the rate-limiting step's energy requirement (CO* + H* \rightarrow CHO*). On the contrary, the energy barrier of the speed limiting step for C_2H_4 production (CO* + CO* \rightarrow OCCO*) is reduced. (Fig. 7d)

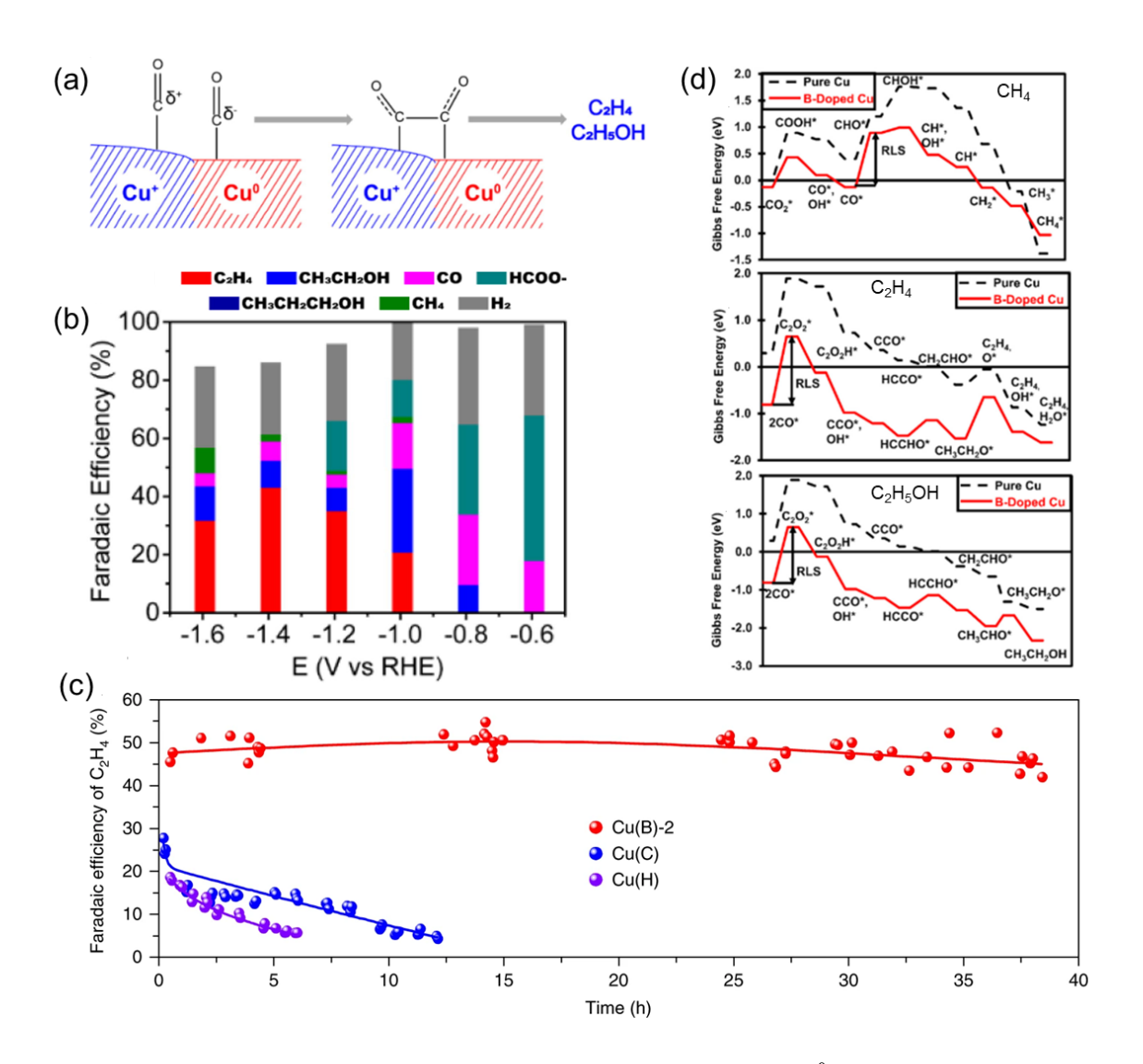


Fig. 7. (a) Schematic illustration for C₂ production at surface Cu⁺/Cu⁰ sites on Cu-Cu₂O catalyst.

(b) FE for all products on Cu/Cu₂O nanorods. (a-b) Reproduced with permission. ¹¹² Copyright 2019, Elsevier. (c) FE of ethylene on Cu(B)-2, Cu(C), and Cu(H) in long-time testing. (d) DFT calculations on reaction energy diagrams for CO₂ conversion to CH₄, C₂H₄, and C₂H₅OH on a pure Cu (111) facet and a B-doped Cu (111) surface. (c-d) Reproduced with permission. ⁸⁵ Copyright 2018, Nature Publishing Group.

Metal/metal compounds core/shell catalysts (such as Sn) with compound shell reduced to zero-valent metals during the reaction may increase the number of active sites for the CO_2RR . Sn/SnS₂ core/shell nanosheets produced formic acid at low potentials of -0.23 V vs. RHE with FE up to 84.5% at -0.68 V vs. RHE. ¹¹⁴ The reduced metallic Sn from SnS₂ under cathodic conditions serves as the catalytic site. The increase in formic acid yield was attributed to the residue of SnS₂, where the sulfide ion (S²⁻) adsorbed on the metal surface would inhibit the adsorption of *COOH intermediate. Since CO_2 reduction to CO_2 is the rate-determining step at metallic Sn electrodes ¹¹⁵, DFT calculations indicated that, when CO_2 bonds a *p*-block element like S, a separately occupied *p* orbital can stabilize the electrons localized in the $2p_z$ orbital of C associated with CO_2 .

Core/shell nanowire arrays with Ag cores and metal shells might produce better performance than spherical NPs due to efficient electron transfer. Vertical Ag/AgCl core/shell nanowire (Ag/AgCl_x CSNW) arrays were prepared on the Ag foil through low-temperature nano-imprinting technology and rapid surface chlorination to form thin AgCl shells. The FE_{CO} of Ag/AgCl_x CSNWs can reach 91% at the low overpotential of -0.46 V vs. RHE, and approximately 20% can be

detected at the initial potential of -0.3 V vs. RHE. The high conductivity of Ag promotes electron transfer, and the partially reduced AgCl_x shell exposes a large number of active sites (grain boundaries and defects). DFT calculations indicated that AgCl is more favorable for adsorption of *COOH as opposed to Ag.

4.3 Metal compound/metal or metal compound core/shell structures

Designing a metal compound core to adjust the metal or metal compound shell's oxidation state and electronic structure is another strategy to improve CO_2RR performance. 8.5 nm core/shell NPs composed of a Cu_2S core and a Cu vacancy shell were synthesized and can improve C_{2+} alcohol products (ethanol and propanol), with the FE of C_{2+} alcohols reaching $32 \pm 1\%$ (Fig. 8a-b).¹⁹ DFT calculations illuminated that, in pure copper, ethylene's kinetic energy barriers (0.560 eV) and ethanol (0.645 eV) generation are quite similar. When a Cu vacancy exists, and S is introduced into the subsurface (Cu_2S/Cu core/shell structure), the kinetic energy barrier of ethylene increases significantly (1.148 eV), but that of ethanol is mostly unaffected (0.427 eV), thereby improving the selectivity of alcohol products.

In the previous section, we showed that the Cu⁺ surface could improve the efficiency of multicarbon products. Introducing N into the core to regulate the metal surface's oxidation state and electronic structure is a feasible method. A 3 nm Cu surface layer was deposited on Cu₃N and Cu₂O to prepare Cu₃N/Cu (Fig. 8c) and Cu₂O/Cu core/shell NPs. For Cu₃N/Cu, the content of Cu⁰ is increased and that of Cu₃N is decreased during the initial 60 min electrolysis. After that, the catalyst gradually reaches a stable surface composition with a partial oxidation state of the surface Cu layer (± 0.25 valence state). At ± 0.95 V vs. RHE, the Cu₃N/Cu gives the highest C₂₊ production (FE_{C2+} = 64%, where FE_{ethylene} = 39%, FE_{ethanol} = 19%), much higher than those of pure Cu and Cu₂O/Cu catalysts (Fig. 8d-e). Cu at the surface of a Cu₃N/Cu catalyst produces the highest oxidation state and could reduce C-C dimerization's energy barrier, which was significantly lower than the Cu and Cu₂O/Cu structures.

Producing surface defects and/or forming surface oxidation are recently found to boost CO₂RR performance. 8.0 nm AuFe/Au core/shell NPs (AuFe-CSNP) were prepared by a hot solvent method (produce AuFe alloy) and subsequent electrolysis to leach the surface Fe, which can generate a large amount of CO at low potential (-0.2 V vs. RHE). The maximum FECO of these AuFe-CSNPs reaches 97.6% at -0.4 V. 59 Leaching the surface Fe leads to the formation of a core/shell structure with a jagged surface enriching a large number of vacancies and active sites. DFT calculations and analysis of free energy changes disclosed that the formation energy of *COOH is decreased by 0.19 eV after the formation of sawtooth surfaces and vacancies, resulting in the enhanced CO production. Jiao et al. prepared AgSn/SnO_x core/shell NPs with a 1.7 nm SnO_x layer by a galvanic displacement method and its maximum FE_{HCOOH} reached 87.2% at -0.9 V vs. RHE. 118 Compared to the formation of *COOH, the formation of OCHO* is facilitated by the presence of oxygen vacancies in surface SnO_x, thereby improving the selectivity of HCOOH. Cu₂O/SnO₂ core/shell nanocubes were prepared and the catalyst with a 5 nm SnO₂ shell demonstrated the highest FE_{CO}, reaching 90.9% at -0.9 V vs. RHE.¹¹⁹ The original cubic structure

is not retained and decomposes into assemblies of smaller nanoparticles with distinctly exposed Cu/Sn grain boundaries. The excellent performance for CO generation may be due to the synergistic effect between Cu and Sn atoms.

This section discusses the core/shell structures for the CO₂RR with three categories. Their structure-dependent catalytic performance is listed in Table 3. Overall, with an optimization, the introduction of strain effects could effectively change the catalyst surface's electronic structure to lower the reaction energy barrier for the CO₂RR. Besides, tuning the vacancies and valance states of shell metals produces a synergistic effect with the corresponding core to tailor the reaction pathway, especially for C₂₊ product formation.

Table 3. Summary of representative core/shell structured bimetallic catalysts for CO₂RR.

Core	Shell	Products	Efficiency	Potential	Refs.	
	Metal/metal core/shell structures					
Au	Pd	СО	96.7%	-0.6 V vs. RHE	106	
Pt	Au	$\mathrm{CH_4}$	32%	-1.0 V vs. RHE	120	
		C_2H_4	10%	-0.8 V vs. RHE		
Ag	Cu-7	CO	82%	-1.06 V vs. RHE	107	
	Cu-20	C_2H_4	28.6%	-1.06 V vs. RHE		
Au	Cu	C_2H_4	20%	-0.6 V vs. RHE	108	
	Metal/metal compound core/shell structures					
Cu	SnO ₂	СО	70%	-0.7 V vs. RHE	109	
		НСООН	71.5%	-1.0 V vs. RHE		
Cu	SnO_2	CO	90.2%	-1.0 V vs. RHE	94	
Cu	SnO_2 -0.8nm	CO	93%	-0.7 V vs. RHE	13	
	SnO_2 -1.8nm	НСООН	85%	-0.9 V vs. RHE		
Cu	In_2O_3	syngas	~90%		111	
Ag	SnO_2	НСООН	75.1%	-0.9 V vs. RHE	60	
		CO	88%	-0.7 V vs. RHE		
Cu	Cu_2O	C_2	50%	-1.0 V vs. RHE	112	
Cu	CuB	C_2H_4	52±2%	-1.1 V vs. RHE	85	

		C_2H_5OH	27±1%	-1.1 V vs. RHE		
Sn	Sn_2S	НСООН	84.5%	-0.68 V vs. RHE	97	
Ag	AgCl	CO	91%	-0.46 V vs. RHE	116	
	Metal compound/metal or metal compound core/shell structures					
Cu ₂ S	Cu	C_2H_4	42%	-1.1 V vs. RHE	19	
		C_2H_5OH	15±1%	-0.95 V vs. RHE		
		C_3H_7OH	$8\pm0.7\%$	-0.95 V vs. RHE		
Cu_3N	Cu	C_2H_4	39±2%	-0.95 V vs. RHE	117	
		C_2H_5OH	19±1%	-0.95 V vs. RHE		
		C_3H_7OH	6±1%	-0.95 V vs. RHE		
AuFe	Au	CO	97.6%	-0.4 V vs. RHE	59	
Ag_3Sn	SnO_2	НСООН	87.2%	-0.9 V vs. RHE	118	
Cu ₂ O	SnO_2	CO	90.9%	-1.0 V vs. RHE	119	

Core/shell structured catalysts have been extensively studied for the CO₂RR and a wide range of catalytic products (basically covers all products of C₁ and C₂) have been reported. Generally, the selectivity of CO and HCOOH can reach 90% based on SnO₂ shell, and the highest C₂₊ product can reach 80% with a shell of Cu-based catalysts. Most of the above-mentioned core/shell structured catalysts are composed of oxide or sulfide shells, which are not stable and would be reduced during the CO₂RR testing. Such reduction process would lead to the reconstruction of catalyst surface and generate low valence state or metallic metals, vacancies, and defects, which, in turn, serve as new active sites. However, it will also bring complexity to the mechanism research. In the future, in-situ spectroscopic and structural characterizations can be utilized to identify and determine the actual catalytic sites evolved during the reaction and the reaction mechanism. For industrial applications under high current densities, the reduction of surface compounds might be intensified, which would cause the collapse of the core/shell structures and the change of active

species. Improving the structural stability of catalysts and achieving industrial standards will be future directions.

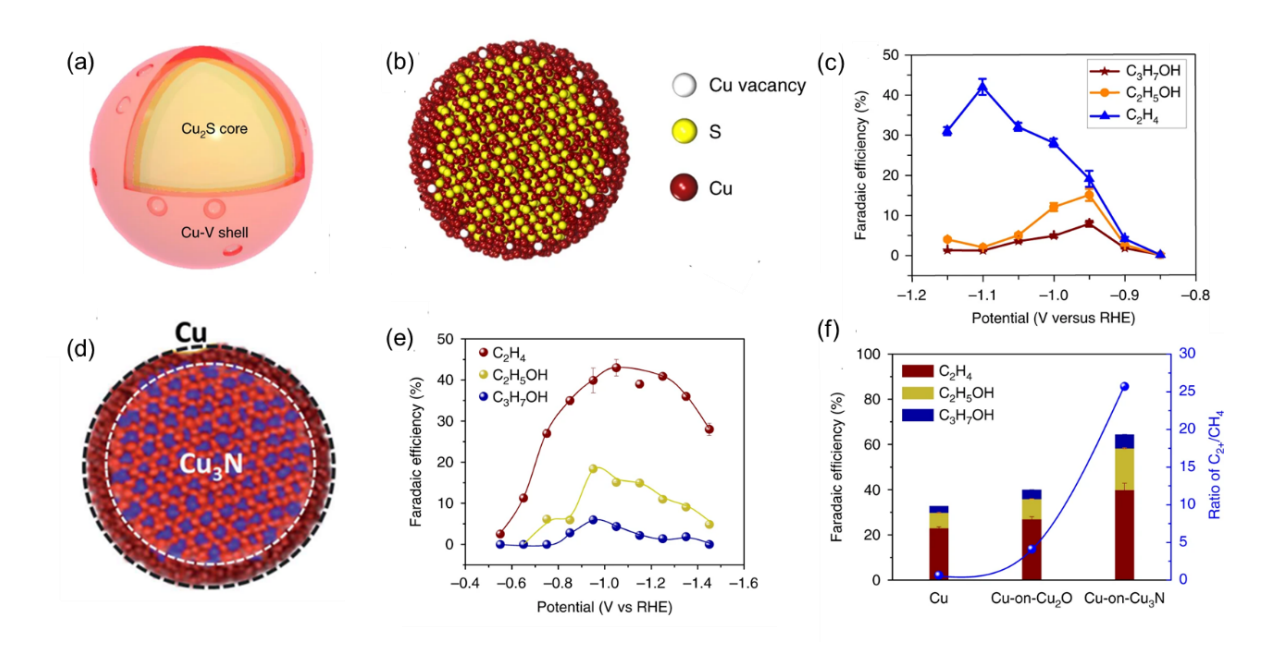


Fig. 8. (a) Schematic and (b) atomoc model of the Cu₂S-Cu-V structure. (c) FEs of ethylene, ethyl alcohol and propyl alcohol on Cu₂S-Cu-V. (a-c) Reproduced with permission. ¹⁹ Copyright 2018, Nature Publishing Group. (d) Schematic of the Cu₃N/Cu catalyst. (e) FEs of C₂ and C₃ products on the Cu₃N/Cu catalyst. (f) Comparison of FE for C₂₊ and the ratio of C₂₊/CH₄ at -0.95 V vs. RHE on Cu, Cu₂O/Cu, and Cu₃N/Cu. (d-f) Reproduced with permission. ¹¹⁷, Copyright 2018, Nature Publishing Group.

5. Phase separated bimetallic nanocatalysts for the CO₂RR

Phase-separated structures can also enhance the CO₂RR through heterogeneous synergistic effects.

First, the active sites st the two-phase interfaces have the advantages of small steric hindrance and short migration distance, which is beneficial for the coupling of varied intermediates. Second, lattice distortion at the interfaces provides a large number of active sites and charge accumulated, which is a feasible way to optimize the binding of intermediates. CuPd phase-separated NPs were prepared through co-reduction of Pd(II) acetate, and Cu(II) acetate by using NaBH₄ as a reducing agent⁶⁵ The phase-separated samples consist of two aggregates with different morphologies: (1) spherical particles with ~ 50 nm and (2) an interconnected structure composed of ~ 20 nm particles. The phase-separated CuPd NPs exhibited a maximum FE_{C2} of 63%, superior to homogeneous CuPd NPs. The neighboring characteristics of Cu atoms existing in the phase-separated CuPd NPs can provide suitable molecular distance and small steric hindrance, facilitating the dimerization of adjacently adsorbed CO to C₂ products.

Phase separated Cu₃Sn/Cu₆Sn₅ catalysts were developed by electrochemical deposition of Sn on Cu foam (to form intermetallic Cu-Sn with atomic ratios of 3/1 and 6/5) followed by a thermal annealing (Fig. 9a-b).⁵⁷ The Cu₃Sn/Cu₆Sn₅ phase-separated structure demonstrated a maximum FE_{HCOOH} of 82% at -1.0 V vs. RHE with good stability. In contrast, the main products on the individual Cu₃Sn and Cu₆Sn₅ alloy catalysts are primarily H₂ under the same conditions. DFT calculations predicted that, on the Cu₃Sn/Cu₆Sn₅, the adsorption energy of HCOO* was more negative than that of COOH* and the energy difference between HCOO* and COOH* for the phase-separated structure is larger than that for the individual Cu₃Sn or Cu₆Sn₅. Also, the Gibbs free energy of the HER on the Cu₃Sn/Cu₆Sn₅ (-0.28 eV) is less negative than Cu₃Sn (-1.09 eV)

and Cu₆Sn₅ (-0.52 eV) (Fig. 9c-d), suggesting an inhibition to the HER.

Phase separated structures can produce a two-phase interface containing a heterogeneous synergistic effect to influence reaction intermediates' adsorption behaviors and the favorable reaction pathway. Although few studies on the phase-separated structure can achieve a selectivity of more than 60% in the preparation of C₂ products. There are two kinds of the active site in the phase-separated structures: the surface of each phase and the interface between the two phases. However, the interaction of these two types of active sites on the catalytic pathways is still unclear. Advanced phase separated structures with more favorable sites/inferaces exposed should be designed and prepared in the future. Also, in-situ characterizations could elucidate the synergistic effect on the two-phase interface and its impact on reaction mechanisms.

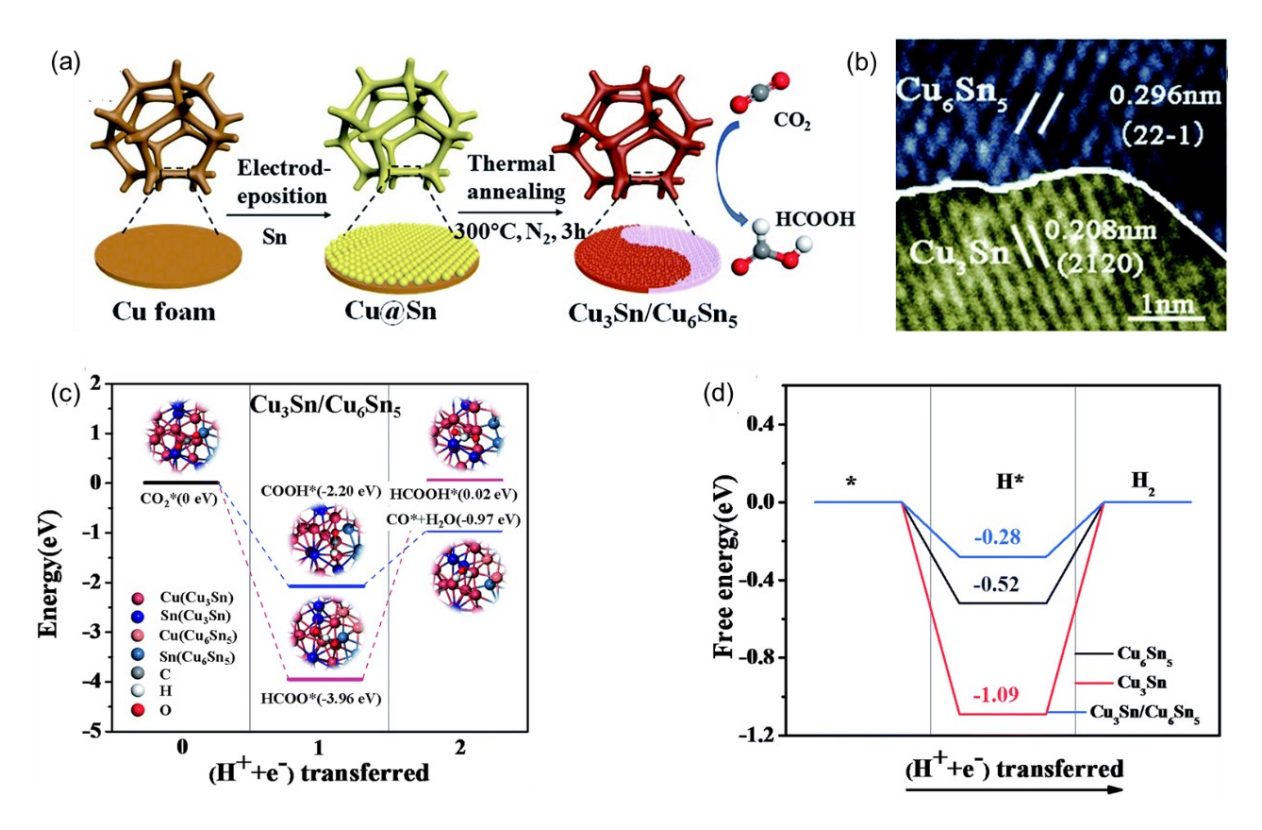


Fig. 9. (a) Schematic illustration of heterostructured Cu₃Sn/Cu₆Sn₅ preparation on Cu foam. (b)

HRTEM image of CuSn phase-separated structure. (c-d) Calculated free energy diagrams of (c) CO₂RR and (d) HER on Cu₃Sn/Cu₆Sn₅. (a-d) Reproduced with permission.⁵⁷ Copyright 2019, Royal Society of Chemistry.

6. Summary and Outlook

Electrochemical conversion of CO₂ into highly-valued chemicals is a promising strategy to alleviate environmental issues by mitigating excessive CO₂ content in the atmosphere. To achieve highly efficient and selective electrocatalytic CO₂ reduction, rationally designed electrocatalysts with optimized electronic and geometric structures are incredibly essential. In this review, we focus on bimetallic catalysts, one of the most promising catalysts for the CO2RR, including intermetallic, core-shell structure, and phase-separated catalysts concerning atomic arrangement engineering. Intermetallic catalysts are thermodynamically stable and have unique electronic structure and welldefined coordination environments, thereby efficiently catalyzing CO₂ reduction with enhanced activity, selectivity, and stability. In core/shell structures, adjusting surface electronic structures by the strain effect and introducing more active sites by tuning shell vacancies/valence states could generate a favorable synergistic effect to enhance the CO₂RR. For phase-separated structures, the existence of heterogeneous phase interfaces with different chemical properties may assist in the combination of different intermediates and reduce the electron migration distance at the phase interface, resulting in improved catalytic activity and product selectivity.

Although current progress in developing various bimetallic catalysts is very encouraging,

there is still a large gap between the currently achieved efficiency and the possible commercial applications. Future researches on the CO₂RR will focus on the following aspects:

- (i) Due to the complexity of the CO₂RR, it is necessary to have a deeper understanding of the reaction mechanism and provide theoretical guidance for the design of high-performance catalysts. Full descriptions of the interactions involving active sites, surrounding reactants/solvents, and adsorbed intermediates are still very challenging. With theoretical calculations and modeling, it will be easier to acquire a more detailed understanding of critical products' reaction pathways and determine various intermediates' thermodynamic parameters.
- (ii) Regarding working conditions under reductive potentials, structure changes of catalysts during the CO₂RR should be more scrutinized. In-situ and operando characterization such as X-ray absorption spectroscopy could provide more insight into the catalyst structure's evolution throughout the catalytic process. Overall, the correlated investigation on theory and characterization is crucial to moving this field forward.
- (iii) Based on increased awareness of the reaction mechanism and structure evolution, the synthesis of a catalyst with precisely designed composition, morphology, and structure is essential. Preparing model catalysts with well-defined surface electronic and geometric structures at the atomic level should be significantly considered, which is beneficial for progressing the study of relationships between structure and properties.
- (iv) Catalyst researches cannot be limited only to the traditional aqueous electrolytes. Although some of the reported catalysts show excellent performance in an H-cell, there is still a significant

gap to a more realistic solid-state electrolyzer device by using gas diffusion electrodes that can operate at a higher current density. In industrial applications, the minimum current density required for flow cell configurations is estimated to be ~200 mA cm⁻², product selectivity greater than 90%, with acceptable stability over thousands of hours.^{121, 122} At present, a part of bimetallic catalysts can maintain high selectivity over 10 h under the condition of high current densities. Long-term durability, which is the biggest problem hindering the applications of catalysts from the laboratory to the industry, would focus on future research. Cost is another consideration for catalyst industrialization, which currently ranges from \$0.21 to \$2.1 kg⁻¹ for typical CO₂RR products (such as CO, HCOOH, CH₄, C₂H₄, etc.).¹²² Reducing precious metal usage and designing efficient and durable non-precious metal catalysts is a feasible way to mitigate catalyst cost.

Acknowledgment

This work was financial supported by the National Nature Science Foundation of China (21972051) (Q.L). G. Wu acknowledges the support from National Science Foundation (CBET-1604392, 1804326). D.D would like to acknowledge the support by Idaho National Laboratory Directed Research and Development Program under DOE Idaho Operations Office under contract no. DE-AC07-05ID14517.

References

- 1. D. H. Nam, P. De Luna, A. Rosas-Hernandez, A. Thevenon, F. Li, T. Agapie, J. C. Peters, O. Shekhah, M. Eddaoudi and E. H. Sargent, *Nat. Mater.*, 2020, **19**, 266-276.
- 2. Y. Li, H. Wang, C. Priest, S. Li, P. Xu and G. Wu, Adv. Mater., 2021, 33, 2000381.
- 3. L. Zhang, Z. J. Zhao and J. Gong, Angew. Chem. Int. Ed., 2017, 56, 11326-11353.
- 4. M. Mikkelsen, M. Jørgensen and F. C. Krebs, *Energy Environ. Sci.*, 2010, **3**, 43-81.

- 5. S. X. Guo, Y. Zhang, X. Zhang, C. D. Easton, D. R. MacFarlane and J. Zhang, *ChemSusChem*, 2019, **12**, 1091-1100.
- 6. Y. Wang, J. Liu, Y. Wang, A. M. Al-Enizi and G. Zheng, Small, 2017, 13.
- 7. D. D. Zhu, J. L. Liu and S. Z. Qiao, Adv. Mater., 2016, 28, 3423-3452.
- 8. J. Yano and S. Yamasaki, J. Appl. Electrochem., 2008, 38, 1721-1726.
- 9. K.-C. Cheung, P. Guo, M.-H. So, L. Y. S. Lee, K.-P. Ho, W.-L. Wong, K.-H. Lee, W.-T. Wong, Z.-Y. Zhou and K.-Y. Wong, *J. Organometallic Chem.*, 2009, **694**, 2842-2845.
- 10. L. Liu and Y. Li, Aerosol Air Quality Res., 2014, 14, 453-469.
- 11. M. Li, B. Hua, L.-C. Wang, Z. Zhou, K. J. Stowers and D. Ding, *Catal. Today*, 2020, DOI: <u>10.1016/j.cattod.2020.1004.1059</u>.
- 12. H. Zhang, J. Li, Q. Tan, L. Lu, Z. Wang and G. Wu, Chem. Euro. J. 2018, 24, 18137-18157.
- 13. Q. Li, J. Fu, W. Zhu, Z. Chen, B. Shen, L. Wu, Z. Xi, T. Wang, G. Lu, J. J. Zhu and S. Sun, *J. Am. Chem. Soc.*, 2017, **139**, 4290-4293.
- 14. Q. Shao, P. Wang, S. Liu and X. Huang, *J. Mater. Chem. A*, 2019, 7, 20478-20493.
- 15. L. Jia, H. Yang, J. Deng, J. Chen, Y. Zhou, P. Ding, L. Li, N. Han and Y. Li, *Chin. J. Chem.*, 2019, **37**, 497-500.
- 16. S. Liu, X. F. Lu, J. Xiao, X. Wang and X. W. D. Lou, *Angew. Chem. Int. Ed.*, 2019, **58**, 13828-13833.
- 17. Y. Pang, J. Li, Z. Wang, C.-S. Tan, P.-L. Hsieh, T.-T. Zhuang, Z.-Q. Liang, C. Zou, X. Wang, P. De Luna, J. P. Edwards, Y. Xu, F. Li, C.-T. Dinh, M. Zhong, Y. Lou, D. Wu, L.-J. Chen, E. H. Sargent and D. Sinton, *Nat. Catal.*, 2019, **2**, 251-258.
- 18. Hyung Mo Jeong, Youngkook Kwon, Jong Ho Won, Yanwei Lum, Mu-Jeng Cheng, Kwang Ho Kim, Martin Head-Gordon and J. K. Kang, *Adv. Energy Mater.*, 2020, **10**, 1903423.
- 19. T.-T. Zhuang, Z.-Q. Liang, A. Seifitokaldani, Y. Li, P. De Luna, T. Burdyny, F. Che, F. Meng, Y. Min, R. Quintero-Bermudez, C. T. Dinh, Y. Pang, M. Zhong, B. Zhang, J. Li, P.-N. Chen, X.-L. Zheng, H. Liang, W.-N. Ge, B.-J. Ye, D. Sinton, S.-H. Yu and E. H. Sargent, *Nat. Catal.*, 2018, 1, 421-428.
- Y. C. Li, Z. Wang, T. Yuan, D. H. Nam, M. Luo, J. Wicks, B. Chen, J. Li, F. Li, F. P. G. de Arquer, Y. Wang, C. T. Dinh, O. Voznyy, D. Sinton and E. H. Sargent, *J. Am. Chem. Soc.*, 2019, 141, 8584-8591.
- 21. R. Kortlever, I. Peters, C. Balemans, R. Kas, Y. Kwon, G. Mul and M. T. Koper, *Chem. Commun.*, 2016, **52**, 10229-10232.
- 22. A. S. Varela, N. Ranjbar Sahraie, J. Steinberg, W. Ju, H. S. Oh and P. Strasser, *Angew. Chem. Int. Ed.*, 2015, **54**, 10758-10762.
- 23. B. Kumar, M. Asadi, D. Pisasale, S. Sinha-Ray, B. A. Rosen, R. Haasch, J. Abiade, A. L. Yarin and A. Salehi-Khojin, *Nat. Commun.*, 2013, 4.
- 24. H. Zhang, Y. Ma, F. Quan, J. Huang, F. Jia and L. Zhang, *Electrochem. Commun.*, 2014, 46, 63-66.
- 25. F. Zhu, K. Tu, L. Huang, X. Qu, J. Zhang, H. Liao, Z. Zhou, Y. Jiang and S. Sun, *Electrochim. Acta*, 2018, **292**, 208-216.
- 26. N. Mohd Adli, W. Shan, S. Hwang, W. Samarakoon, S. Karakalos, Y. Li, D. A. Cullen, D. Su, Z. Feng, G. Wang and G. Wu, *Angew. Chem. Int. Ed.*, 2021. **60**. 1022-1032.
- 27. Z. Li, A. Cao, Q. Zheng, Y. Fu, T. Wang, K. T. Arul, J.-L. Chen, B. Yang, N. M. Adli, L. Lei, C.-L. Dong, J. Xiao, G. Wu and Y. Hou, *Adv. Mater.*, 2011, **33**, 2005113.
- 28. F. Pan, H. Zhang, K. Liu, D. Cullen, K. More, M. Wang, Z. Feng, G. Wang, G. Wu and Y. Li, *ACS Catal.*, 2018, **8**, 3116-3122.
- 29. H. Xie, T. Wang, J. Liang, Q. Li and S. Sun, *Nano Today*, 2018, **21**, 41-54.
- 30. T. Wang, Q. Zhao, Y. Fu, C. Lei, B. Yang, Z. Li, L. Lei, G. Wu and Y. Hou, *Small Methods*, 2019, **3**, 1900210.
- 31. Q. Shi, S. Hwang, H. Yang, F. Ismail, D. Su, D. Higgins and G. Wu, *Mater. Today*, 2020, **37**, 93-111.
- 32. X. Wang, Q. Zhao, B. Yang, Z. Li, Z. Bo, K. H. Lam, N. M. Adli, L. Lei, Z. Wen, G. Wu and Y. Hou, *J. Mater. Chem. A*, 2019, 7, 25191-25202.
- 33. H. Park, J. Choi, H. Kim, E. Hwang, D.-H. Ha, S. H. Ahn and S.-K. Kim, Appl. Catal. B

- Environ., 2017, 219, 123-131.
- 34. S. Zhao, R. Jin and R. Jin, ACS Energy Lett., 2018, 3, 452-462.
- 35. P. Deng, H. Wang, R. Qi, J. Zhu, S. Chen, F. Yang, L. Zhou, K. Qi, H. Liu and B. Y. Xia, *ACS Catal.*, 2019, **10**, 743-750.
- 36. J. Gu, F. Heroguel, J. Luterbacher and X. Hu, Angew. Chem. Int. Ed., 2018, 57, 2943-2947.
- 37. Z. Chen, T. Fan, Y.-Q. Zhang, J. Xiao, M. Gao, N. Duan, J. Zhang, J. Li, Q. Liu, X. Yi and J.-L. Luo, *Appl. Catal. B Environ.*, 2020, **261**, 118243.
- 38. R. M. Arán-Ais, F. Scholten, S. Kunze, R. Rizo and B. R. Cuenya, *Nat. Energy*, 2020, **5**, 317-325.
- 39. S. Back, J. H. Kim, Y. T. Kim and Y. Jung, *Phys. Chem. Chem. Phys.*, 2016, 18, 9652-9657.
- 40. Z. Chen, T. Fan, Y.-Q. Zhang, J. Xiao, M. Gao, N. Duan, J. Zhang, J. Li, Q. Liu, X. Yi and J.-L. Luo, *Appl. Catal. B Environ.*, 2020, **261**.
- 41. S. Sen, D. Liu and G. T. R. Palmore, ACS Catal., 2014, 4, 3091-3095.
- 42. F. S. Roberts, K. P. Kuhl and A. Nilsson, *Angew. Chem. Int. Ed.*, 2015, **54**, 5179-5182.
- 43. D. Ren, B. S.-H. Ang and B. S. Yeo, ACS Catal., 2016, **6**, 8239-8247.
- 44. M. Armbru ster, Kirill Kovnir, Malte Behrens, Detre Teschner, Yuri Grin and R. Schlo gl, J. Am. Chem. Soc., 2010, 132, 14745-14747
- 45. M. Armbruster, G. Wowsnick, M. Friedrich, M. Heggen and R. Cardoso-Gil, *J. Am. Chem. Soc.*, 2011, **133**, 9112-9118.
- 46. María Escudero-Escribano, Paolo Malacrida, Martin H. Hansen, Ulrik G. Vej-Hansen, Amado Velázquez-Palenzuela, Vladimir Tripkovic, Jakob Schiøtz, Jan Rossmeisl, Ifan E. L. Stephens and I. Chorkendorff, *Science*, 2016, **352**.
- 47. Sho Iihama, Shinya Furukawa and T. Komatsu, ACS Catalysis, 2016, 6, 742–746.
- 48. Y. Zhu, J. Sokolowski, X. Song, Y. He, Y. Mei and G. Wu, *Adv. Energy Mater.*, 2020, **10**, 1902844.
- 49. J. Jiang, K. Zhao, X. Xiao and L. Zhang, J. Am. Chem. Soc., 2012, 134, 4473-4476.
- 50. B.-W. Zhang, Y.-X. Jiang, J. Ren, X.-M. Qu, G.-L. Xu and S.-G. Sun, *Electrochim. Acta*, 2015, **162**, 254-262.
- 51. X. Bai, W. Chen, C. Zhao, S. Li, Y. Song, R. Ge, W. Wei and Y. Sun, *Angew. Chem. Int. Ed.*, 2017, **56**, 12219-12223.
- 52. Q. Li, Y. Zhang, X. Zhang, H. Wang, Q. Li, J. Sheng, J. Yi, Y. Liu and J. Zhang, *Ind. Eng. Chem. Res.*, 2019, DOI: 10.1021/acs.iecr.9b03017.
- 53. J. E. Pander, M. F. Baruch and A. B. Bocarsly, ACS Catalysis, 2016, 6, 7824-7833.
- 54. C. Cui, J. Han, X. Zhu, X. Liu, H. Wang, D. Mei and Q. Ge, J. Catal., 2016, 343, 257-265.
- 55. A. Klinkova, P. De Luna, C.-T. Dinh, O. Voznyy, E. M. Larin, E. Kumacheva and E. H. Sargent, ACS Catal., 2016, 6, 8115-8120.
- 56. S. Zhang, P. Kang and T. J. Meyer, J. Am. Chem. Soc., 2014, 136, 1734-1737.
- 57. J. Jiao, R. Lin, S. Liu, W. C. Cheong, C. Zhang, Z. Chen, Y. Pan, J. Tang, K. Wu, S. F. Hung, H. M. Chen, L. Zheng, Q. Lu, X. Yang, B. Xu, H. Xiao, J. Li, D. Wang, Q. Peng, C. Chen and Y. Li, *Nat. Chem.*, 2019, **11**, 222-228.
- 58. Y. Chen, C. W. Li and M. W. Kanan, *J. Am. Chem. Soc.*, 2012, **134**, 19969-19972.
- 59. K. Sun, T. Cheng, L. Wu, Y. Hu, J. Zhou, A. Maclennan, Z. Jiang, Y. Gao, W. A. Goddard, 3rd and Z. Wang, *J. Am. Chem. Soc.*, 2017, **139**, 15608-15611.
- 60. J. Zhang, M. Qiao, Y. Li, Q. Shao and X. Huang, ACS Appl. Mater. Interfaces, 2019, 11, 39722-39727.
- 61. M. Wencka, J. Kovač, V. D. B. C. Dasireddy, B. Likozar, A. Jelen, S. Vrtnik, P. Gille, H. J. Kim and J. Dolinšek, *J. Analy. Sci. Techno.*, 2018, **9**.
- 62. R. Kortlever, J. Shen, K. J. Schouten, F. Calle-Vallejo and M. T. Koper, *J. Phys. Chem. Lett.*, 2015, **6**, 4073-4082.
- 63. N. J. Firet and W. A. Smith, ACS Catal., 2016, 7, 606-612.
- 64. C. W. Li and M. W. Kanan, J. Am. Chem. Soc., 2012, 134, 7231-7234.
- 65. S. Ma, M. Sadakiyo, M. Heima, R. Luo, R. T. Haasch, J. I. Gold, M. Yamauchi and P. J. Kenis, *J. Am. Chem. Soc.*, 2017, **139**, 47-50.

- 66. J. H. Lee, S. Kattel, Z. Jiang, Z. Xie, S. Yao, B. M. Tackett, W. Xu, N. S. Marinkovic and J. G. Chen, *Nat. Commun.*, 2019, **10**, 3724.
- 67. D. Kim, J. Resasco, Y. Yu, A. M. Asiri and P. Yang, *Nat. Commun.*, 2014, **5**, 4948.
- 68. J. D. Goodpaster, A. T. Bell and M. Head-Gordon, J. Phys. Chem. Lett., 2016, 7, 1471-1477.
- 69. E. Perez-Gallent, M. C. Figueiredo, F. Calle-Vallejo and M. T. Koper, *Angew. Chem. Int. Ed.*, 2017, **56**, 3621-3624.
- 70. A. Dutta, M. Rahaman, N. C. Luedi, M. Mohos and P. Broekmann, *ACS Catal.*, 2016, **6**, 3804-3814.
- 71. A. D. Handoko, K. W. Chan and B. S. Yeo, *ACS Energy Lett.*, 2017, **2**, 2103-2109.
- 72. L. R. L. Ting and B. S. Yeo, Curr. Opinion in Electrochem., 2018, **8**, 126-134.
- 73. D. A. Porter, M. Sherif and K.E.E., *Third Edition (CRC Press)*, 2009.
- 74. B. Hammer, *Topics in Catal.*, 2006, **37**, 3-16.
- 75. J. K. Norskov, T. Bligaard, J. Rossmeisl and C. H. Christensen, Nat. Chem., 2009, 1, 37-46.
- 76. J. Liang, F. Ma, S. Hwang, X. Wang, J. Sokolowski, Q. Li, G. Wu and D. Su, *Joule*, 2019, **3**, 956-991.
- 77. J. Liang, S. Li, Y. Chen, X. Liu, T. Wang, J. Han, S. Jiao, R. Cao and Q. Li, *J. Mater. Chem. A*, 2020, **8**, 15665-15669.
- 78. T. Wang, J. Liang, Z. Zhao, S. Li, G. Lu, Z. Xia, C. Wang, J. Luo, J. Han, C. Ma, Y. Huang and Q. Li, *Adv. Energy Mater.*, 2019, **9**.
- 79. J. Liang, Z. Zhao, N. Li, X. Wang, S. Li, X. Liu, T. Wang, G. Lu, D. Wang, B. J. Hwang, Y. Huang, D. Su and Q. Li, *Adv. Energy Mater.*, 2020, DOI: 10.1002/aenm.202000179.
- 80. J. Liang, N. Li, Z. Zhao, L. Ma, X. Wang, S. Li, X. Liu, T. Wang, Y. Du, G. Lu, J. Han, Y. Huang, D. Su and Q. Li, *Angew. Chem. Int. Ed.*, 2019, **58**, 15471-15477.
- 81. M. V. Lebedeva, V. Pierron-Bohnes, C. Goyhenex, V. Papaefthimiou, S. Zafeiratos, R. R. Nazmutdinov, V. Da Costa, M. Acosta, L. Zosiak, R. Kozubski, D. Muller and E. R. Savinova, *Electrochim. Acta*, 2013, **108**, 605-616.
- 82. D. Wang, H. L. Xin, R. Hovden, H. Wang, Y. Yu, D. A. Muller, F. J. DiSalvo and H. D. Abruna, *Nat. Mater.*, 2013, **12**, 81-87.
- 83. T. Bligaard and J. K. Nørskov, *Electrochim. Acta*, 2007, **52**, 5512-5516.
- 84. M. Mavrikakis, B. Hammer and J. K. Nørskov, *Phy. Rev. Lett.*, 1998, **81**, 2819 2822.
- 85. Y. Zhou, F. Che, M. Liu, C. Zou, Z. Liang, P. De Luna, H. Yuan, J. Li, Z. Wang, H. Xie, H. Li, P. Chen, E. Bladt, R. Quintero-Bermudez, T. K. Sham, S. Bals, J. Hofkens, D. Sinton, G. Chen and E. H. Sargent, *Nat. Chem.*, 2018, **10**, 974-980.
- 86. M. Karamad, V. Tripkovic and J. Rossmeisl, ACS Catal., 2014, 4, 2268-2273.
- 87. D. J. V. Emerilis Casado-Rivera, Laif Alden, Cora Lind, Craig Downie, Terannie Vázquez-Alvarez, Antonio C. D. Angelo, Francis J. DiSalvo, and Héctor D. Abruña, *J. Am. Chem. Soc.*, 2004, **126**, 4043-4049.
- 88. D. He, L. Zhang, D. He, G. Zhou, Y. Lin, Z. Deng, X. Hong, Y. Wu, C. Chen and Y. Li, *Nat. Commun.*, 2016, 7, 12362.
- 89. A. Groß, *Topics in Catal.*, 2006, **37**, 29-39.
- 90. J. R. Kitchin, J. K. Norskov, M. A. Barteau and J. G. Chen, *Phys. Rev. Lett.*, 2004, **93**, 156801.
- 91. A. Schlapka, M. Lischka, A. Gross, U. Kasberger and P. Jakob, *Phys. Rev. Lett.*, 2003, 91, 016101.
- 92. Y. Gauthier, M. Schmid, S. Padovani, E. Lundgren, V. Bus, G. Kresse, J. Redinger and P. Varga, *Phys. Rev. Lett.*, 2001, **87**, 036103.
- 93. L. Bu, S. Guo, X. Zhang, X. Shen, D. Su, G. Lu, X. Zhu, J. Yao, J. Guo and X. Huang, *Nat. Commun.*, 2016, 7, 11850.
- 94. J. Wang, Y. Ji, Q. Shao, R. Yin, J. Guo, Y. Li and X. Huang, *Nano Energy*, 2019, **59**, 138-145.
- 95. K. D. Gilroy, A. Ruditskiy, H. C. Peng, D. Qin and Y. Xia, *Chem. Rev.*, 2016, **116**, 10414-10472.
- 96. B. T. Sneed, C. N. Brodsky, C. H. Kuo, L. K. Lamontagne, Y. Jiang, Y. Wang, F. F. Tao, W. Huang and C. K. Tsung, *J. Am. Chem. Soc.*, 2013, **135**, 14691-14700.
- 97. D. Kim, C. Xie, N. Becknell, Y. Yu, M. Karamad, K. Chan, E. J. Crumlin, J. K. Norskov and P. Yang, *J. Am. Chem. Soc.*, 2017, **139**, 8329-8336.

- 98. W. Zhao, L. Yang, Y. Yin and M. Jin, J. Mater. Chem. A, 2014, 2, 902-906.
- 99. A. M. Ismail, G. F. Samu, A. Balog, E. Csapó and C. Janáky, *ACS Energy Lett.*, 2018, **4**, 48-53.
- 100. A. A. Peterson and J. K. Nørskov, *J. Phys. Chem. Lett.*, 2012, **3**, 251-258.
- 101. M. Yamauchi and T. Tsukuda, *Dalton Trans.*, 2011, **40**.
- 102. D. A. Torelli, S. A. Francis, J. C. Crompton, A. Javier, J. R. Thompson, B. S. Brunschwig, M. P. Soriaga and N. S. Lewis, *ACS Cataly.*, 2016, **6**, 2100-2104.
- 103. Y. Hori and A. Murata, *Electrochim. Acta*, 1990, **35**, 1777-1780.
- 104. A. R. Paris and A. B. Bocarsly, *ACS Catal.*, 2017, **7**, 6815-6820.
- H. A. Hansen, J. B. Varley, A. A. Peterson and J. K. Norskov, *J. Phys. Chem. Lett.*, 2013, 4, 388-392.
- 106. S. Zhu., X. Qin., Q. Wang., T. Li., R. Tao., M. Gu. and M. Shao, *J. Mater. Chem. A*, 2019, 7, 16954–16961.
- 107. Z. Chang, S. Huo, W. Zhang, J. Fang and H. Wang, *J. Phys. Chem. C*, 2017, **121**, 11368-11379.
- 108. J. Monz'o., Y. Malewski., R. Kortlever., F. J. Vidal-Iglesias., J. Solla-Gull'on., M. T. M. Koper. and P. Rodriguez., *J. Mater. Chem. A*, 2015, **3**, 23690–23698.
- 109. P. Wang, M. Qiao, Q. Shao, Y. Pi, X. Zhu, Y. Li and X. Huang, *Nat. Commun.*, 2018, **9**, 4933.
- J. Wang, Y. Ji, Q. Shao, R. Yin, J. Guo, Y. Li and X. Huang, *Nano Energy* 2019, 59, 138–145.
- 111. H. Xie, S. Chen, F. Ma, J. Liang, Z. Miao, T. Wang, H. L. Wang, Y. Huang and Q. Li, *ACS Appl. Mater. Interfaces*, 2018, **10**, 36996-37004.
- 112. L. Shang, X. Lv, H. Shen, Z. Shao and G. Zheng, *J. Colloid Interface Sci.*, 2019, **552**, 426-431.
- 113. H. Xiao, T. Cheng and W. A. Goddard, 3rd, *J Am Chem Soc*, 2017, **139**, 130-136.
- 114. F. Li, L. Chen, M. Xue, T. Williams, Y. Zhang, D. R. MacFarlane and J. Zhang, *Nano Energy*, 2017, **31**, 270-277.
- 115. Y. Hori, *Springer*, 2008.
- 116. Junyu Ge, Jun Long, Zixu Sun, Han Feng, Jie Hu, See Wee Koh, Qing Yu, Jianping Xiao and H. Li, *ACS Appl. Energy Mater.*, 2019, **2**, 6163–6169.
- 117. Z. Q. Liang, T. T. Zhuang, A. Seifitokaldani, J. Li, C. W. Huang, C. S. Tan, Y. Li, P. De Luna, C. T. Dinh, Y. Hu, Q. Xiao, P. L. Hsieh, Y. Wang, F. Li, R. Quintero-Bermudez, Y. Zhou, P. Chen, Y. Pang, S. C. Lo, L. J. Chen, H. Tan, Z. Xu, S. Zhao, D. Sinton and E. H. Sargent, *Nat. Commun.*, 2018, **9**, 3828.
- 118. W. Luc, C. Collins, S. Wang, H. Xin, K. He, Y. Kang and F. Jiao, *J. Am. Chem. Soc.*, 2017, **139**, 1885-1893.
- 119. S.-N. Zhang, M. Li, B. Hua, N. Duan, S. Ding, S. Bergens, K. Shankar and J.-L. Luo, *ChemCatChem*, 2019, **11**, 4147–4153.
- 120. Rulle Reske, Matteo Duca, Mehtap Oezaslan, Klaas Jan P. Schouten, Marc T. M. Koper and P. Strasser, *J. Phys. Chem. Lett.*, 2013, **4**, 2410 2413.
- 121. R. Lin, J. Guo, X. Li, P. Patel and A. Seifitokaldani, *Catalysts*, 2020, 10.
- 122. S. Verma, B. Kim, H. R. Jhong, S. Ma and P. J. Kenis, *ChemSusChem*, 2016, **9**, 1972-1979.

